JOURNAL OF GEOPHYSICAL RESEARCH, VOL. 110, C05017, doi:10.1029/2004JC002468, 2005

# Modeling and measurement of sediment transport by waves in the vortex ripple regime

A. G. Davies
School of Ocean Sciences, University of Wales, Bangor, Anglesey, UK

P. D. Thorne
Proudman Oceanographic Laboratory, Liverpool, UK

Received 6 May 2004; revised 16 November 2004; accepted 10 March 2005; published 24 May 2005.

[1] Above steep, wave-induced sand ripples, which occur extensively in shallow sea areas, the momentum transfer and suspended sediment dynamics are dominated by the formation and shedding at flow reversal of lee wake vortices. Since two-dimensional models of this process are unduly complex for practical application, a simple, one-dimensional vertical (1DV), two-layer, model is presented here for the flow and transport above such ripples. In the lower layer of thickness equal to two ripple heights, vortex shedding is represented by a time-varying eddy viscosity with peak values at flow reversal while, in the upper layer, a standard turbulence-closure formulation is used. Suspended sediment is introduced at the ripple crest by a time-varying pick-up function. The ripple dimensions and suspended grain size are also predicted. The model results are compared with data obtained beneath weakly asymmetrical waves in a large-scale flume. Intrawave measurements of suspended concentration were obtained using an acoustic backscatter system, and sediment profiles obtained above different locations on a moving rippled-bed profile are used to provide intraripple and ripple-averaged descriptions of the intrawave concentration field for comparison with the model. The results of a harmonic analysis suggest that the mean component and second harmonic (two-peak symmetry term) of the concentration are well predicted, particularly near the bed. The modeled wave-related component dominates the net sand transport rate; near-bed transport is in the onshore direction, while transport in the outer boundary layer is offshore. The new 1DV formulation provides a simple, but realistic, modeling approach for the rippled regime.

**Citation:** Davies, A. G., and P. D. Thorne (2005), Modeling and measurement of sediment transport by waves in the vortex ripple regime, *J. Geophys. Res.*, *110*, C05017, doi:10.1029/2004JC002468.

## 1. Introduction

[2] One of the largely unsolved problems in the modeling of sand transport by waves and currents is how best to represent, within a simplified framework, the essentially two- (or three-) dimensional mechanism of lee-wake vortex shedding and the associated sediment entrainment above a rippled bed. Over large areas of the continental shelf, outside the surf zone, the seabed is covered with wave-formed sand ripples. If the steepness $\eta/\lambda$ ($\eta$ = ripple height, $\lambda$ = ripple wavelength) of these oscillatory ripples exceeds about 0.1, the boundary layer separates behind the crests and vortex formation and shedding occurs during each wave half cycle [*Sleath*, 1984]. This phenomenon gives rise to a fundamentally different spatial and temporal distribution of momentum transfer in the near seabed layer compared with that above a flat (nonrippled) bed in oscillatory flow. The pick-up of sediment from a rippled bed is also fundamentally different, being associated mainly with vortex shedding at about the instants of flow reversal; in contrast, above a flat bed, maximum pick-up occurs at times of peak bed shear stress. Importantly, the shed vortices are highly effective in transporting sediment to far greater heights above a rippled bed than occurs above plane beds where no such coherent mechanism is present. Since rippled beds occur in relatively low wave conditions, this can lead to the paradoxical outcome that, for a given mean current strength, more sand may be transported in the presence of small waves above rippled beds than by sheet flow beneath large waves above plane beds [*Davies and Villaret*, 2002].

[3] Equilibrium ripples with two-dimensional (i.e., long-crested) profiles, formed by low waves in the laboratory, typically have steepness $0.15 > \eta/\lambda > 0.25$ [*Sleath*, 1984], and occur in the parameter ranges (1) "relative roughness" $A_1/k_s \sim O(1)$ and (2) Reynolds number $RE = A_1U_1/\nu \sim O(10^3-10^4)$, where $U_1$ is the near-bed velocity amplitude, $A_1$ ($= U_1/\omega$ where $\omega$ is the angular frequency) is the near-bed excursion amplitude, $k_s$ is the equivalent bed roughness (defined later in terms of $\eta$ and $\lambda$), and $\nu$ is the kinematic viscosity of water. In the field, and also in large-scale laboratory experiments, such as considered in this paper,


0148-0227/05/2004JC002468$09.00

steep ripples can be found at values of $RE \sim O(10^5)$. As the waves become more active, the ripple steepness decreases ($0.05 < \eta/\lambda < 0.15$, $A_1/k_s \sim O(10)$), the ripples gradually become washed out ($\eta/\lambda < 0.05$, $A_1/k_s \sim O(10-10^2)$), and eventually the bed becomes plane ($\eta/\lambda \rightarrow 0$, $A_1/k_s \sim O(10^2-10^3)$, $RE \sim O(10^6-10^7)$). Roughly speaking, vortex shedding from the ripple crests begins when $\eta/\lambda > 0.10$, and may be considered to be fully developed when $\eta/\lambda \approx 0.12-0.13$ [*Davies and Villaret*, 1997]. For ripple steepness $\eta/\lambda < 0.10$, vortex shedding does not occur to a significant extent and the bed may be considered to be "dynamically plane" [*Davies and Villaret*, 2002]. The mechanisms of sediment transport above the respective bed types depend primarily on the parameters indicated above, together with the sediment grain size and its distribution. These mechanisms are moderated significantly, however, by any asymmetry in the wave motion, as discussed later for weakly asymmetric surface waves. Asymmetry in the wave-induced flow not only influences the strength and nature of the vortices formed above the ripple lee-slopes, but also affects the amount of sediment "pick-up" in the two halves of the wave cycle.

[4] Reviews concerning sand concentrations and transport in oscillatory flow above rippled beds have been provided by *Fredsøe and Deigaard* [1992], *Nielsen* [1992], *Van Rijn* [1993], and, more recently, *Van Rijn et al.* [2001]. The basic characteristics of the instantaneous, local sand concentration field over ripple profiles were demonstrated in the laboratory by *Bosman* [1982], *Block et al.* [1994] and *Villard and Osborne* [2002], and in the field by *Vincent et al.* [1999], among others. The process of vortex formation and shedding was quantified by *Marin* [1988], *Ranasoma* [1992], and *Earnshaw* [1996], while averaged flow properties were studied experimentally by *Lofquist* [1980] and *Rankin and Hires* [2000]. As far as the equivalent bed roughness ($k_s$) in wave and current flows above steep ripples is concerned, most measurements suggest that $k_s \approx 3\eta-4\eta$, where $\eta$ is the ripple height. *Mathisen and Madsen* [1996a, 1996b, 1999] carried out comprehensive studies of $k_s$ in the laboratory, while *Styles and Glenn* [2002] proposed models for the prediction of both the ripple dimensions and the bed roughness, which they validated using field data.

[5] In relation to sediment transport, intrawave measurements of sediment entrainment and suspension, made over a full ripple wavelength, are rather scarce [*Sato and Horikawa*, 1986; *Sato et al.*, 1987]. On small laboratory scales, only a limited number of point measurements have usually been obtained, typically made with optical probes above the ripple crest and trough [*Nakato et al.*, 1977; *Block et al.*, 1994]. *Sleath and Wallbridge* [2002] used a digital video camera to study pick-up rates from rippled beds in oscillatory flow, and assessed the quasi-steady nature of the flow in the very near-bed mobile layer. In larger scale experiments involving rippled beds, acoustic probes have been used to measure the instantaneous concentration and velocity components beneath regular and irregular waves [*Chung and Van Rijn*, 2003], and high-resolution acoustic backscatter systems (ABS) have been used to study time variations in concentration on longer wave-group scales [*Vincent and Hanes*, 2002]. *Thorne et al.* [2002, 2003a, 2003b] reported ABS measurements made in the large-scale Deltaflume of Delft Hydraulics above steeply rippled sand beds. The experiments reported by *Thorne et al.* [2003b] comprised detailed intrawave measurements made above different locations on a (migrating) rippled bed.

[6] For beds that are steeply rippled, two-dimensional horizontal-vertical (2DHV) modeling studies have sought to represent the formation and shedding of vortices, and the subsequent trajectories of the (decaying) vortices. The models include numerical solutions of the governing vorticity equation [*Sleath*, 1973, 1982; *Blondeaux and Vittori*, 1991], discrete-vortex models [*Longuet-Higgins*, 1981; *Block et al.*, 1994; *Hansen et al.*, 1994; *Perrier et al.*, 1995; *Malarkey and Davies*, 2002] and turbulence-closure models [*Lewis et al.*, 1995; *Perrier*, 1996; *Andersen and Fredsøe*, 1999; *Trouw et al.*, 2000]. *Andersen et al.* [2001] used a $k$-$\omega$ turbulence-closure model to show that the instantaneous stresses over a ripple surface are typically several times larger than those on a flat bed, while *Andersen and Faraci* [2003] recently used the same model to study wave-current interaction above ripples in general angular cases. At a more fundamental level, large eddy simulation (LES) has started to be used for the flow above ripples. *Zedler and Street* [2001] found evidence from a LES of the importance of coherent, three-dimensional (3D), flow structures for sediment entrainment in steady flow above ripples. More recently, *Watanabe et al.* [2003] used a LES to study 3D-vortex structures above steeply rippled beds in oscillatory flow, and suggested that these structures may be responsible for enhancing the suspension and convection of sediments. The direct numerical simulation (DNS) of *Scandura et al.* [2000] provided further insight into 3D mixing effects in oscillating flow above ripples. As far as sediment in suspension above ripples is concerned, Lagrangian particle tracking has been used in several oscillatory flow models [e.g., *Hansen et al.*, 1994; *Block et al.*, 1994; *Perrier*, 1996].

[7] Although 2D models have achieved reasonable success in representing the main features of vortex dynamics and the associated sediment transport above rippled beds, these models are unduly complex and computationally demanding from an engineering point of view. For practical purposes it is desirable, therefore, to formulate a model that both captures the essential physics of the vortex shedding process, and is also sufficiently simple, and computationally undemanding, to be run over wide (wave, current and sediment) parameter ranges of practical importance. Existing one-dimensional vertical (1DV) models fail to meet the first of these requirements, usually attempting to represent ripples simply by enhancing the roughness ($k_s$) used in standard, 1DV "flat bed" formulations. While this approach has some merit for low ripples ($\eta/\lambda < 0.1$) [*Davies and Villaret*, 2002], it has severe limitations for steep ripples [*Eidsvik*, 2004; *Malarkey and Davies*, 2004]. *Nielsen* [1992], *Chung and Van Rijn* [2003], and *Chung et al.* [2000] have shown that an unsteady, 1DV ripple-averaged approach can yield good wave period-averaged sand concentrations. However, the potentially important wave-related component of the suspended transport cannot be simulated accurately, at least using conventional flat-bed modeling concepts.

[8] For 1DV modeling above rippled beds, fundamentally different formulations are required for the eddy viscosity

($K$) and sediment diffusivity ($K_s$). *Sleath* [1991] and *Nielsen* [1992] proposed height-invariant formulations for the time-mean eddy viscosity ($\overline{K}$) in the near-bed, vortex-dominated layer. This structure represents the fact that, while the turbulent mixing length scale increases with height above the bed, the turbulent velocity scale decreases inversely with height [*Sleath*, 1991]; the eddy viscosity, being characterized by the product of these two scales, therefore remains constant with height, at least in a near-bed layer. Sleath's formulation for $\overline{K}$ was compared with field data by *Smyth et al.* [2002]. *Nielsen* [1992] related the time-mean diffusivity $\overline{K}_s$ to $\overline{K}$ by an empirical constant $\beta = \overline{K}_s/\overline{K}$ ($\approx$ 3–4). *Van Rijn* [1993] also used a height-invariant diffusivity in the lowest layer of a three-layer formulation. Subsequently, it was shown by *Perrier et al.* [1995] on the basis of a Reynolds-stress closure model, and by *Davies and Villaret* [1997, 1999] with reference to the laboratory data of *Ranasoma and Sleath* [1992], that time variation in the eddy viscosity is more pronounced above ripples than above plane beds, with peaks in viscosity occurring near times of flow reversal. This 1DV eddy viscosity approach, and its extension to the simulation of sediment pick-up by ejected vortices, was used by *Davies and Thorne* [2002] to study time-averaged features of sediment transport by waves and currents above ripples, and it also forms the basis for the present paper.

[9] While most simplified 1DV formulations have been based upon turbulent-diffusion concepts, *Nielsen* [1992] developed an alternative approach, involving combined convection and diffusion, for steeply rippled beds above which eddy shedding occurs. Nielsen's convection-diffusion approach was used by, for example, *Lee and Hanes* [1996] in comparisons with field data, and was assessed by *Thorne et al.* [2002] in connection with acoustic (ABS) data obtained above steep ripples. The latter found that measured mean concentration profiles could be represented well by use of (a rescaled version of) *Nielsen*'s [1992] pure convection and combined convection-diffusion approaches. They argued further, however, that the same results could be obtained, at least for the time-mean concentration profile, by use of diffusion concepts, provided that the eddy viscosity included a height-invariant near-bed layer [cf. *Van Rijn*, 1993; *Davies and Villaret*, 1997] or, alternatively, a "constant + linear" near-bed eddy viscosity structure.

[10] The accurate prediction of the net sand transport rate in the rippled bed regime beneath waves remains an important objective. Quasi-steady models developed for the wave-related transport above flat beds have also been used for this purpose in the ripple regime, for example, the Bagnold-Bailard model [*Bailard*, 1981; *Bailard and Inman*, 1981]. This type of model generally yields net transport in the (onshore) wave direction [e.g., *Houwman and Ruessink*, 1996]. An exception is the model of *Sato and Horikawa* [1986] which produces net offshore-directed transport beneath asymmetrical waves in the ripple regime, in accordance with experiment. This issue was addressed by *Nielsen* [1988] who proposed three practical modeling approaches for the prediction of net transport rates by asymmetrical waves above rippled beds, including a simple, but effective, "grab and dump" model. The net transport in each model was in the "offshore" direction, i.e., in the direction opposite to that of the largest (absolute) velocity.

[11] The motivation for the present paper is to present a relatively simple, 1DV modeling approach for oscillatory flow, and the associated sand transport, above steep vortex ripples, together with validation of the model using data obtained in a large-scale wave flume. In section 2 the formulation of the new 1DV, two-layer, model is discussed. This model comprises a lower, near-bed, layer of thickness equal to 2 ripple heights in which the process of vortex shedding is represented by a strongly time-varying eddy viscosity having its peak values close to the instants of flow reversal in the free stream. In the upper layer, the model reverts to a standard 1DV turbulence-closure formulation, subject to appropriate matching conditions with the lower vortex layer. Sediment transport is driven by a strongly time-varying pick-up function defined at the ripple crest level. Other processes included in the model are a prediction scheme for the ripple dimensions, and a procedure for the calculation of the suspended sediment grain size. In section 3, a series of detailed intrawave measurements is presented of the suspended concentration and associated velocity field. The observations were made beneath weakly asymmetrical waves above a bed of medium sand in a large-scale flume, and included measurements of the ripple dimensions. The suspended concentrations were measured with an acoustic backscatter system (ABS) above a mobile rippled bed, allowing intrawave sediment profiles to be obtained above different locations on the moving bed profile, i.e., intraripple measurements. A key element in the present analysis has involved the horizontal averaging of these profiles, to provide a ripple-averaged description of the intrawave concentration field. In section 4, the 1DV model results are compared with the measured, ripple-averaged concentrations. Both time-mean and intrawave comparisons are presented, including a harmonic analysis of both the model results and the measurements. The discussion of the results focuses on the extent to which the new model captures the principal features of the intrawave suspended sediment concentrations, the harmonic analysis allowing a critical assessment to be made of the model's performance. In section 5, the implications of the results are discussed for the prediction of net sand transport rates beneath waves, and broader issues relating to convection versus diffusion in the wave boundary layer, and the relationship between the sediment diffusivity and eddy viscosity, are discussed. The conclusions of the study are presented in section 6.

## 2. The 1DV Model of Oscillatory Flow Above Vortex Ripples

[12] The present model is an extension of the one-dimensional vertical (1DV), turbulence-closure model of *Davies and Li* [1997]. Its key new feature is an analytical, near-bed, submodel that represents the processes of vortex shedding, and the associated entrainment of sediment at times of flow reversal. In this lower layer, the model solves the time-dependent, phase-ensemble momentum equation for the horizontally averaged velocity, and the continuity equation for the horizontally averaged suspended sediment concentration, both quantities having been horizontally averaged over a ripple wavelength. In the upper layer, above this vortex-dominated region, the model reverts to a standard turbulence-closure formulation, subject to matching condi-

tions for velocity, turbulent energy, eddy viscosity, and sediment concentration, at a level corresponding to two ripple-heights above the (undisturbed) mean bed level.

### 2.1. Model Background

[13] In two-dimensional, turbulent oscillatory flows, the instantaneous local velocity components ($u$-horizontal, $w$-vertical) may be decomposed into phase-ensemble components ($u_p$, $w_p$) and turbulent components ($u'$, $w'$), e.g. $u = u_p + u'$. (Ensemble averaging with regard to the phase is assumed to have been carried out here over a sufficiently large number of wave cycles to yield a velocity field comprising the time-mean and time-varying periodic (or wave) components only.) Further, we neglect the viscous stresses and write the phase-ensemble momentum balance in the horizontal $x$-direction, including advection terms, as follows [c.f. *Nielsen*, 1992]:

$$\frac{\partial u_p}{\partial t} + u_p \frac{\partial u_p}{\partial x} + w_p \frac{\partial u_p}{\partial z} = \frac{\partial U_\infty}{\partial t} - \frac{\partial}{\partial x}\left(u'^2\right)_p - \frac{\partial}{\partial z}\left(u'w'\right)_p, \quad (1)$$

where $x$ and $z$ are the horizontal and vertical axes, $t$ is the time, $U_\infty(t)$ is the free-stream velocity, and $(u'^2)_p$ and $(u'w')_p$ are the normal and tangential components of the phase-ensemble turbulent Reynolds stress. The boundary layer is here assumed to be thin, and the pressure gradient across it is assumed to be zero. The components ($u_p$, $w_p$) are related by the continuity equation

$$\frac{\partial u_p}{\partial x} + \frac{\partial w_p}{\partial z} = 0. \quad (2)$$

For a rippled bed of wavelength $\lambda$, we define horizontally averaged (over the ripple length) variables as functions of time and distance from the bed as below, for example, for the horizontal velocity,

$$\langle u_p \rangle = \frac{1}{\lambda}\int_0^\lambda u_p dx. \quad (3)$$

After horizontally averaging in this way, equation (1) subject to the continuity equation (2) reduces to the linearized wave boundary layer equation normally associated with a flat bed,

$$\frac{\partial \langle u_p \rangle}{\partial t} = \frac{dU_\infty}{dt} + \frac{\partial}{\partial z}\left(\frac{\tau_p}{\rho}\right), \quad (4)$$

but in which

$$\frac{\tau_p}{\rho} = -\left\langle (u'w')_p \right\rangle - \langle u_p w_p \rangle. \quad (5)$$

Here the total shear stress $\tau_p$ is made up of two components. The first is the horizontally averaged, turbulent Reynolds stress, and the second is the horizontally averaged momentum transfer associated with periodic velocity correlations. It is this latter contribution that makes the dominant contribution in the near-bed layer above ripples. This was shown by *Perrier et al.* [1995], who horizontally averaged the results from a Reynolds-stress closure model of the flow above steep ripples, and found that the "periodic stress" term in equation (5) was a factor of 5 times larger than the "turbulent stress" term. *Sleath* [1987] had earlier noted the same effect experimentally above a very rough bed in oscillatory flow.

[14] By analogy with the gradient diffusion assumption, we here assume that the total stress $\tau_p$ in the near-bed layer, which is mainly due to periodic velocity contributions ($\tau_p \approx -\rho\langle u_p w_p \rangle$), can be related to the mean flow velocity gradient ($\partial\langle u_p\rangle/\partial z$) by an eddy viscosity coefficient $K(z, t)$, as follows:

$$\tau_p = \rho K \frac{\partial \langle u_p \rangle}{\partial z}. \quad (6)$$

As far as the volumetric suspended sediment concentration $c$ is concerned, the same ripple-averaging procedure may be used, such that the 1DV sediment continuity equation becomes

$$\frac{\partial \langle c \rangle}{\partial t} = \frac{\partial}{\partial z}\left(w_s \langle c \rangle + K_s \frac{\partial \langle c \rangle}{\partial z}\right), \quad (7)$$

where $w_s$ is the settling velocity of a single sediment particle, and $K_s$ is the sediment diffusivity.

### 2.2. Eddy Viscosity in Oscillatory Flow Above Ripples

[15] The structure of the eddy viscosity is based, in the first place, on the findings for symmetrical waves of *Perrier et al.* [1995] and also *Davies and Villaret* [1997]. *Perrier et al.* [1995] found that having horizontally averaged the results from both a Reynolds-stress closure model and also a discrete-vortex model, the vertical profiles of time-varying velocity and shear stress were coherent and bore some similarity to the classical vertical profiles associated with a Stokes shear wave above a plane bed. Analysis of these vertical profiles showed that (1) the magnitude of the eddy viscosity $K$ was roughly height constant and (2) the phase relationship between the mean velocity gradient and the mean shear stress was such that the eddy viscosity coefficient $K$ was strongly time varying with peak values centered on times of flow reversal in the free stream. This structure, which differs qualitatively from the time-varying structure of K above a plane bed [e.g., *Trowbridge and Madsen*, 1984], was found by *Perrier et al.* [1995] to be present in a layer of thickness equivalent to about $2\eta$. *Andersen and Faraci* [2003], using a $k$-$\omega$ model for combined wave and current flow, found that the total wave boundary layer thickness was equivalent typically to about $5\eta$, within which variation associated with vortex effects took place in approximately the bottom $2\eta$. Similar results were obtained recently by *Malarkey and Davies* [2004], who horizontally averaged the results from a discrete-vortex model, and found strong peaks in the eddy viscosity at times of flow reversal (i.e., at approximately the time of vortex ejection from the bed [see also *Malarkey and Davies*, 2002]). Closer inspection of the phase angle of the peak in eddy viscosity, obtained with $A_1/k_s = 1.25$ by both *Perrier et al.* [1995] and *Malarkey and Davies* [2004], reveals that while the peak in $K$ is centered on flow reversal, there is a gradual phase shift, such that the peak occurs somewhat

after reversal at a height of about $^1\!/_2\eta$ above the ripple crest level, and before reversal, above this, at a height of about $2\eta$ above the crest. This counterintuitive behavior is qualitatively different from that expected above a plane bed, and perhaps helps to explain later the observed variation with height of the phase angle of the measured suspended sediment concentration field (see section 4).

[16] *Davies and Villaret* [1997] analyzed the laboratory data of *Ranasoma and Sleath* [1992] and confirmed the existence of a height-independent, strongly time-varying eddy viscosity with peaks at flow reversal. However, owing to the lack of vertical resolution in the data, they did not find any evidence of a phase shift in $K$ with increasing height. *Davies and Villaret* [1999] used this formulation for $K$ to study the Eulerian drift above ripples and, from analysis of a number of published laboratory data sets involving weakly asymmetrical surface waves, they inferred the asymmetrical behavior for $K$ used in this paper. It should be noted here that the analysis of *Davies and Villaret* [1999] included the effects of streaming associated with vertical wave velocities, as well as residual currents caused by asymmetry effects. Here, in contrast, the governing equations do not include vertical wave velocities. Moreover, the present model uses (in the outer layer) a turbulence-closure formulation that does not include streaming, and so it is only residual currents generated by asymmetry effects that are computed. The implications of the neglect of streaming are discussed in section 5.

[17] It is not at all obvious that the gradient diffusion assumption in equation (6) should have any relevance in the oscillatory boundary layer above ripples. As pointed out by *Rodi* [1984], the eddy viscosity analogy between turbulent and molecular motion cannot be correct, in principle, because the "free paths" of the larger eddies responsible for momentum transfer are, in general, not small compared with the fluid domain. Indeed, this objection to the use of gradient diffusion concepts might be considered particularly relevant here, since the vortices shed from the bed have "trajectories" of the same order as the boundary layer thickness. The justification for the heuristic approach adopted here rests simply upon the coherence of the ripple-averaged stress and velocity fields found in 2DHV models and experiments, and on the logical nature of the 1DV eddy viscosity that may be inferred from these velocity fields (about which further details are presented by *Malarkey and Davies* [2004]). Recently, *Nielsen and Teakle* [2004] have proposed a modified gradient diffusion approach based on a "finite-mixing-length theory."

[18] The eddy viscosity $K$, and hence sediment diffusivity $K_s$, are defined below for the lower and upper layers of the two-layer model. The bottom entrainment condition for sediment is also defined below. The boundary conditions for the velocity are no slip ($\langle u_p \rangle = 0$) at the mean bed level ($z = 0$) [cf. *Davies and Villaret*, 1997, 1999], and zero shear stress ($K\, \partial\langle u_p\rangle/\partial z = 0$) at the mean water surface level ($z = h$). For the sediment concentration, a zero flux condition has been applied at the surface.

### 2.3. Lower Vortex Layer ($z < 2\eta$)

[19] In a layer of approximate thickness $2\eta$, where $\eta$ is the ripple height, the measurements of *Ranasoma and Sleath* [1992] suggested that the effect of turbulent Reynolds stresses is negligible in comparison with momentum transfer associated with coherent vortices. Moreover, for these measurements, *Davies and Villaret* [1997] found that the mean eddy viscosity in this layer was well represented by *Nielsen*'s [1992] height-invariant expression for very rough beds, given by

$$\overline{K} = c_K A_1 \omega k_s, \tag{8}$$

in which the overbar denotes a time average, and where the empirical constant $c_K = 0.004$, and $k_s$ is the equivalent bed roughness, given by

$$k_s = 25\eta\frac{\eta}{\lambda}. \tag{9}$$

Equation (8) may be considered applicable in the near-bed region of very rough turbulent flows having $A_1/k_s < 5$ [*Davies and Villaret*, 1999]. *Davies and Villaret* [1997] also found that the eddy viscosity was strongly time varying, with peaks near the instants of flow reversal in the free stream. Here, for the simulation of (weakly) asymmetrical waves, the eddy viscosity is assumed to be given by the real part of following expression:

$$K = \overline{K}\left((1+\varepsilon_0) + \varepsilon_1 e^{i\omega t} + \varepsilon_2 e^{2i\omega t}\right), \tag{10}$$

in which the respective terms on the right-hand side represent the mean, asymmetric, and symmetric components of $K$ with

$$\begin{aligned} \varepsilon_1 &= |\varepsilon_1| e^{i\varphi_1} \\ \varepsilon_2 &= |\varepsilon_2| e^{i\varphi_2}. \end{aligned} \tag{11}$$

Here the phase angles $\varphi_1$ and $\varphi_2$ allow a phase difference between the maximum free-stream velocity and the respective components of the eddy viscosity. The role of the coefficient $\varepsilon_0$ is explained below.

[20] For asymmetrical wave motion having $B < 0.2$, where $B = |U_2/U_1|$, defined at the edge of the wave boundary layer by

$$U_\infty = U_1 e^{i\omega t} + U_2 e^{2i\omega t}, \tag{12}$$

the analysis of *Davies and Villaret* [1999] suggested that the time-varying components of the eddy viscosity behave in the following manner:

$$|\varepsilon_1| = \begin{cases} 10B & B \le 0.1 \\ 1.0 & B \ge 0.1 \end{cases} \tag{13}$$

$$|\varepsilon_2| = \begin{cases} 1 & B \le 0.1 \\ 1 - \dfrac{40}{3}(B - 0.1) & 0.1 \le B \le 0.15 \\ \dfrac{1}{3} & B \ge 0.15 \end{cases}. \tag{14}$$

They also found that peak eddy viscosity occurs just ahead of flow reversal. Here the following phase relationships have been used for the components of the eddy viscosity in

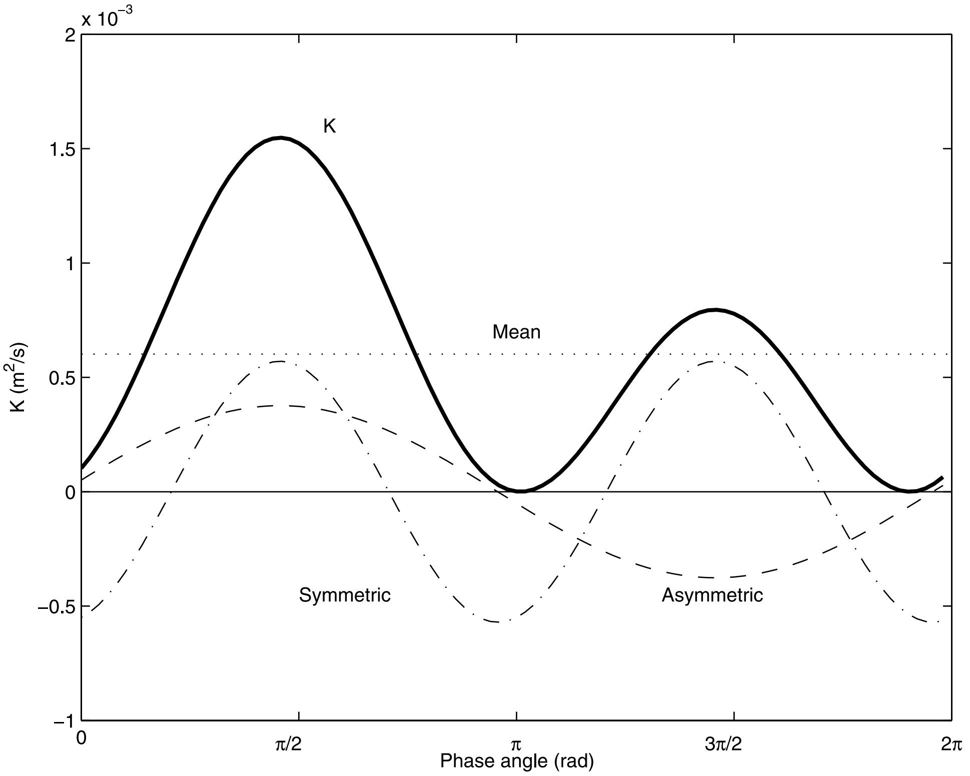


**Figure 1.** Eddy viscosity $K$ (solid line) in the lower vortex layer, together with its components, for a typical asymmetric wave (Test 4). The mean, asymmetric, and symmetric components of $K$ (equation (10)) are shown by the dotted, dashed, and dash-dotted lines, respectively. The corresponding free-stream velocity $U_\infty$, which is given by equation (12) (real part), is shown in Figure 11d.

relation to the instant of flow reversal following the passage of the wave crest [cf. *Davies and Villaret*, 1999],

$$\varphi_2 = 2\varphi_1 \qquad \varphi_1 = -\arccos(B) + \Delta\varphi \tag{15}$$

with the phase lead of peak eddy viscosity ahead of flow reversal corresponding (in radians) to $\Delta\varphi = 4°$. The symmetric term (involving $\varepsilon_2$) in equation (10) dominates the time variation in $K$ for small values of the "asymmetry parameter" $B$. However, as $B$ increases, the asymmetric term (involving $\varepsilon_1$) gradually achieves greater relative importance, reflecting the dominance of the vortex formed beneath the (steep) surface wave crest. In practice, all of the experimental observations discussed later were carried out with weakly asymmetric waves having $B < 0.07$, and so the symmetric effect is always larger than the asymmetric effect.

[21] In the present formulation, the eddy viscosity has been constrained to be positive throughout the wave cycle, as required by the numerical scheme. This has been achieved by the addition, for $B < 0.1$, of a small additive constant in equation (10) given by $\varepsilon_0 = |\varepsilon_1|^2/(8|\varepsilon_2|)$. This constraint did not exist in the analytical study of *Davies and Villaret* [1997], who inferred from the data of *Ranasoma and Sleath* [1992] that the eddy viscosity may even become negative at certain phase instants during the wave cycle. Further, for purposes of the present numerical implementation, in order to achieve a peak value of the eddy viscosity during the wave cycle consistent with the value observed by Ranasoma and Sleath on entering the outer layer ($z > 2\eta$), the empirical constant in *Nielsen*'s [1992] expression (8) has here been rescaled to $c_K = 0.005$ (instead of 0.004), to compensate for the fact that the magnitude of each time-varying component has been "capped" according to equations (13) and (14). (In fact, the numerical values in equations (13) and (14) imply a slightly smaller time variation in $K$ than suggested by *Davies and Villaret* [1999].) Despite these changes, the hydrodynamic model for the lower layer remains closely similar to the formulation proposed by *Davies and Villaret* [1999]. The eddy viscosity $K$ in the lower layer, and its components (equation (10)), are shown in Figure 1 for a typical test that is discussed later.

[22] As far as sediment in suspension in the lower layer is concerned, it has been noted by *Nielsen* [1992], and confirmed by *Thorne et al.* [2002], that the cycle-mean sediment diffusivity $\overline{K}_s$ above ripples is significantly greater than the cycle-mean eddy viscosity $\overline{K}$, such that $\overline{K}_s = \beta\,\overline{K}$, with $\beta > 1$. The reason for this difference has not yet been clearly explained, but presumably rests on the spatial-temporal correlation between locally high (or low) suspended concentrations and locally upward (or downward) vertical velocities in the two- (or three-) dimensional flow field. For purposes of a 1DV model, the $\beta$-effect simply has to be prescribed. *Nielsen* [1992] suggested that the empirical constant $\beta$ was equal to about 4 for rippled beds. In the present study, $\beta$ was treated as a free parameter, but was also found to equal 4 [c.f. *Thorne et al.*, 2002]. An optimized value of $\beta = 4.0$ has been used throughout the present paper.

[23] The bottom boundary condition for sediment has been expressed as a strongly time-varying pick-up function, which represents sediment entrainment associated with the vortex shedding process. In the steady state, the pick-up function must satisfy the time-averaged condition [cf. *Nielsen*, 1992]

$$\overline{-K_s \frac{\partial\langle c\rangle}{\partial z}} = w_s \overline{\langle c\rangle}\ . \tag{16}$$

This condition has been imposed here at the ripple crest level ($z = {}^1\!/_2\eta$), the mean value of the pick-up function being based on *Nielsen*'s [1986] empirical reference concentration formula (see below). As far as time-variation is concerned, the data from the Deltaflume have been used to define the phase angle of sediment pick-up during the wave cycle. According to this data, peak ripple-averaged concentration at the crest level occurs, on average, slightly ahead of the instants of flow reversal in the free stream, and the phase of sediment pick-up has been defined accordingly. Here the instantaneous sediment pick-up is linked to the vortex shedding process, with both $K_s$ and $\partial\langle c\rangle/\partial z$ being time-varying functions. Temporal asymmetry is assumed to arise only by virtue of the asymmetry in the eddy viscosity (equation (10)), and not because of the expression used for the concentration gradient at the crest which is assumed, for simplicity, to be symmetric in time. The assumed pick-up function is given by the real part of

$$\begin{aligned} &-K_s \frac{\partial\langle c\rangle}{\partial z} \\ &\quad = w_s C_0 \frac{\frac{1}{2}\left((1+\varepsilon_0)+\varepsilon_1 e^{i\omega t}+\varepsilon_2 e^{2i\omega t}\right)\left((1+a_c e^{2i\omega t})+c.c.\right)}{\left((1+\varepsilon_0)+\frac{1}{4}A_c|\varepsilon_2|\left(e^{i(2\varphi_1-2\varphi_c)}+c.c.\right)\right)}, \end{aligned} \tag{17}$$

where *c.c.* denotes the complex conjugate. In the quotient on the right hand side of equation (17), the first (complex) term in the numerator arises from the time variation in the eddy viscosity (equation (10)); as noted earlier, this term contains symmetric ($e^{2i\omega t}$) and asymmetric ($e^{i\omega t}$) contributions. The second (real) term in the numerator expresses the assumed time variation in the gradient of concentration at the ripple crest level. This time variation is strong by virtue of the choice of the coefficient $a_c = A_c\exp(2i\varphi_c)$ in which $A_c = 1$. The phase angle $\varphi_c$ has been taken as $\varphi_c = \varphi_1 + 30 \times (\pi/180)$; this corresponds here to $\varphi_c \approx 34°$ and leads to the outcome that the predicted concentration maxima at the crest level occur somewhat ahead of flow reversal. The value of $\varphi_c$, corresponding to the phase lead of concentration gradient over the concentration itself, may be expected to vary in different applications. It should be emphasized that the second term in the numerator includes symmetric time variation but, for simplicity, does not include an asymmetric contribution. The consequences of this are discussed later. Finally, the (real) term in the denominator of the quotient arises simply by virtue of the need to satisfy the time-averaged equation (16). It may be noted that *Nielsen* [1992] has explored the use of a time-varying pick-up function, though this was not linked to a time-varying eddy viscosity of the kind adopted here.

[24] The quantity $C_0$ in equation (17) is the cycle-mean concentration at the crest level, and has been given here by the relationship obtained for the present data by *Thorne et al.* [2002],

$$C_0 = 0.00220\theta_r^3, \tag{18}$$

where the ripple-adjusted value of Shields parameter $\theta_r$ is given, following *Nielsen* [1986], by

$$\theta_r = \frac{\theta'}{\left(1+\pi\frac{\eta}{\lambda}\right)^2}. \tag{19}$$

Here the skin friction Shields parameter $\theta'$ is based on *Swart*'s [1974] friction factor $f_w$, such that

$$\theta' = \frac{f_w U_1^2}{2(s-1)gd_{50}} \qquad f_w = \exp\left[5.213\left(\frac{A_1}{2.5d_{50}}\right)^{-0.194} - 5.977\right], \tag{20}$$

in which $s = \rho_s/\rho$, where $\rho_s$ and $\rho$ are the sediment and fluid densities, respectively (giving $s = 2.65$), $g$ is the acceleration due to gravity, and $d_{50}$ is the median grain diameter of the bed material. The value of the empirical constant in equation (18) differs from *Nielsen*'s [1986] original value of 0.005 for reasons that are discussed later.

### 2.4. Upper Turbulent Layer ($z > 2\eta$)

[25] In the upper layer, the coherent vortex motions are considered to have broken down into random turbulence [cf. *Ranasoma and Sleath*, 1992]. Here the flow is determined by the one-equation turbulence-closure formulation of *Davies and Li* [1997]. Essentially, the horizontally averaged wave boundary layer equation (4) is solved on the basis of an eddy viscosity ($K \sim k^{1/2}\ell$) that is determined from the turbulent kinetic energy (t.k.e., $k$), together with a vertical mixing length scale ($\ell$) based on an extension of Von Karman's similarity hypothesis. The t.k.e. (density) is determined from a standard transport equation, in which the option of turbulence damping by sediment in suspension has here been switched off for simplicity. For brevity, the reader is referred to *Davies and Li* [1997] for details of the formulation. What is important to note here is that matching conditions have been applied at the interface between the lower and upper layers. In particular, at $z = 2\eta$, continuity has been imposed instantaneously in the horizontal velocity $\langle u_p\rangle$, the eddy viscosity $K$, the sediment concentration in suspension $\langle c\rangle$, and the sediment diffusivity $K_s$.

[26] The model runs presented later were carried out with 100 time steps per cycle and 65 vertical intervals distributed on a log linear grid between $z = k_s/30$ and $z = h$. The model was driven by pressure gradients, including first and second harmonic components, where the second harmonic represented the asymmetry in the free-stream motion. (No steady component of the pressure gradient was required in the present runs.) The numerical approach followed essentially that described by *Davies and Li* [1997], subject to the addition of the lower vortex layer. The solution in both (coupled) layers was obtained numerically. At the start of each run, the model procedure was to identify the first grid

level above $z = 2\eta$, which was used as the matching level. Although only those levels lying above $z = 2\eta$ were "active" upper layer levels, the upper layer equations were solved also for the levels below the matching level in order to determine the mixing length ($\ell$) given by the procedure of *Davies and Li* [1997]. Then, on the basis of the (height-invariant) eddy viscosity $K$ in the lower layer (equation (10)), together with the value of $\ell$ at the matching level calculated at each time step, the t.k.e. ($k$) was determined at the matching level, thereby enabling a solution to be obtained numerically in the upper layer. In practice, the value of $\ell$ at $z = 2\eta$ turned out to be about $0.8\eta$ (i.e. $\approx \kappa \times 2\eta$, where $\kappa = 0.4$ is Von Karman's constant). (However, arising from the comments of *Sleath* [1991] about the magnitude of $\ell$, this aspect of the solution may warrant further consideration.)

[27] Finally, in the upper layer, the value of the parameter $\beta$ has been assumed to revert smoothly from its value of 4.0 in the lower layer toward unity according to the power law rule,

$$\beta = 4.0 - 3.0\left(\frac{z - 2\eta}{h - 2\eta}\right)^{\gamma}, \tag{21}$$

where the optimized value $\gamma = 0.4$ has been used here. This procedure represents in some sense the gradual transition from "convective" conditions in the lower layer to more "diffusive" conditions in the upper layer.

### 2.5. Prediction of Ripple Dimensions

[28] The two-layer model described above should be considered applicable if the ripples are "steep," with height ($\eta$) to wavelength ($\lambda$) ratio greater than about 0.12. If the ripple dimensions are known from observation, $\eta$ and $\lambda$ may be imposed as model inputs. However, in general, $\eta$ and $\lambda$ will not be known, and so must be predicted by the model using the hydrodynamic inputs and grain size composition of the bed. The approach adopted here involves use of the formulation of *Wiberg and Harris* [1994] for waves in isolation. In particular, the noniterative procedure described by *Malarkey and Davies* [2003] has been used to determine $\eta$ and $\lambda$. The ripples are predicted to be "orbital," "suborbital," or "anorbital," depending upon the value of the ratio $D_1/d_{50}$ (where $D_1 = 2A_1$ = orbital diameter). The bed roughness ($k_s$) has then been obtained from the ripple dimensions using equation (9).

### 2.6. Suspended Grain Size

[29] The final consideration is the grain size ($d_s$) of the suspended sediment, which also may not be known from observation, compared with the size of the material on the bed (median diameter $d_{50}$). Here the size, and hence settling velocity ($w_s$), of the grains in suspension has been calculated as follows. The peak bed shear stress $\tau'_w$ (skin friction) in the wave cycle and, hence, the (skin) friction velocity $u'_{*w}$ have been estimated using *Swart*'s [1974] formula (equation (20)). Then, on the basis of a lognormal grain size distribution curve [cf. *Li and Davies*, 2001], the largest grain size in suspension (diameter $d_{crit}$) has been estimated by assuming that these grains have settling velocity $w_{s,crit} = 0.8u'_{*w}$ [*Fredsøe and Deigaard*, 1992]. From the resulting size $d_{crit}$, the median diameter $d_s$ of the grains in suspension, and its settling velocity $w_s = w_{s,susp}$ have been estimated using *Soulsby*'s [1997] formula.

[30] Despite the apparently rather large number of empirical parameters in the model formulation, the only truly "free" parameters should be considered to be the magnitude of $a_c$ (namely $A_c$, in equation (17)), the coefficient on the right hand side of equation (18), the power $\gamma$ in equation (21), and the value of $\beta$ in the lower layer (also equation (21)). These quantities have been tuned using the Deltaflume data. All of the remaining empirical quantities have been taken, without further tuning, either from the literature or from previous work by the present authors and collaborators (subject to some minor numerical constraints).

## 3. Experiments With Regular Waves in the Deltaflume

[31] Detailed measurements of sediment in suspension above ripples have been made in the Deltaflume of Delft Hydraulics [*Williams et al.*, 1998]. The large size of this flume (230 m long, 5 m wide, and 7 m deep) allowed the wave and sediment transport phenomena to be studied at full scale. A wave generator at one end of the flume produced regular waves that propagated along the flume and dissipated on a beach at the opposite end. Ten tests are considered here, all carried out with regular, weakly asymmetric waves having heights, $H$, and periods, $T$, in the ranges 0.6–1.3 m and 4–6 s, respectively. Table 1 provides a list of the wave conditions, which were measured by two surface-following wave probes. A sediment bed of thickness 0.5 m and length 30 m was placed approximately halfway along the flume, above which the water depth was 4.5 m in each test. The bed sediment comprised sand of median diameter $d_{50}$ = 0.329 mm, $d_{10}$ = 0.175 mm, and $d_{90}$ = 0.735 mm. To establish equilibrium conditions for the hydrodynamics and sediment transport, the waves propagated over the bed for about 1 hour before data were recorded.

[32] The measurements providing the main focus for the present study were made using an instrumented tripod platform STABLE (Sediment Transport and Boundary Layer Equipment), shown in Figure 2. The main cluster of instruments on STABLE was directed toward the wave generator. This comprised a triple-frequency (1, 2, and 4 MHz) acoustic backscatter system (ABS), with associated pumped sampling, and electromagnetic current meters (ECMs) at three heights above the bed (0.30, 0.61, and 0.91 m). The three ABS transducers were at a height of 1.24 m above the mean bed location, and were aligned parallel to the surface wave crests. The ABS collected backscatter profiles at 128 Hz at each frequency with a resolution of 0.01 m over a range of 1.28 m.

**Table 1.** Deltaflume Parameter Settings[a]

| Test | $H$, m | $T$, s | $\eta$, m | $\lambda$, m |
|---|---|---|---|---|
| 1 | 1.074 | 5 | 0.061 | 0.41 |
| 2 | 1.078 | 5 | 0.059 | 0.41 |
| 3 | 0.811 | 5 | 0.047 | 0.35 |
| 4 | 1.299 | 5 | 0.065 | 0.51 |
| 5 | 1.047 | 5 | 0.046 | 0.38 |
| 6 | 1.064 | 5 | 0.059 | 0.42 |
| 7 | 1.027 | 4 | 0.041 | 0.30 |
| 8 | 0.617 | 6 | 0.040 | 0.28 |
| 9 | 0.971 | 5 | 0.041 | 0.29 |
| 10 | 0.810 | 5 | 0.055 | 0.40 |

[a]Wave height ($h$) and period ($t$), ripple height ($\eta$) and wavelength ($\lambda$).

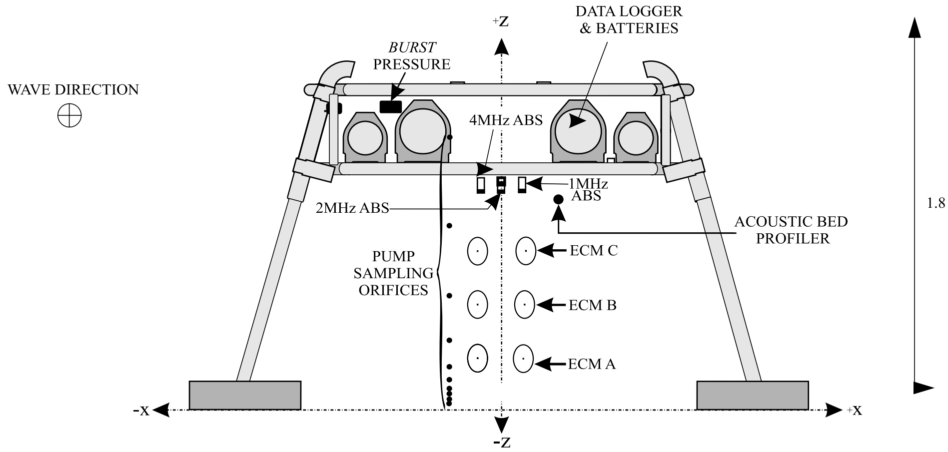


**Figure 2.** Instrumented tripod platform STABLE viewed in the direction of wave propagation. The locations of the triple-frequency ABS, acoustic ripple profiler, electromagnetic current meters, pressure transducer, and pumped sample nozzles (dots) are shown.

The data were block averaged over 32 profiles to give recorded backscatter profiles at 4 Hz at each ABS frequency. The ripples were measured using an acoustic ripple profiler (ARP). Full details of the experimental set up and instrumentation were given by *Thorne et al.* [2002], and the minimal impact that STABLE had on the flow measurements and bed forms was discussed by *Williams et al.* [2003]. The present analysis is concerned with (1) the output from the ABS which provided high-resolution measurements of the suspended concentration, (2) the pumped sample data collected at 10 heights above the bed between 0.05 and 1.55 m, (3) the output from the ARP which gave detailed measurements of the bed morphology, and (4) the hydrodynamic measurements from the ECMs.

[33] Ripples formed on the bed with heights, $\eta$, and wavelengths, $\lambda$, in the respective ranges 0.04–0.07 m and 0.28–0.51 m (see Table 1). The method by which these ranges were determined from the ARP results was described by *Thorne et al.* [2002]. The duration of each test was 1024 s, during the course of which the ripples tended to migrate in the direction of wave propagation. This was reflected by slight asymmetry in the ripple profile shapes.

[34] The bed elevation was also tracked during each test using the backscatter returns at the three ABS frequencies. The nearest range of the bed from the ABS over the experimental recording period of 1024 s was considered to be the “crest” range. It was not always clear from the ABS time series of elevation of bed location that a ripple crest had, in fact, passed beneath a particular transducer since, in some tests, the bed forms migrated by less than a full wavelength during the data collection period. However, for this study we have treated this range as the crest of a ripple. The bed level itself was determined to an accuracy of ±5 mm from a clearly defined echo in the ABS returns [*Thorne et al.*, 2002]. Knowledge of the bed location is obviously vital to any comparison between measured and predicted profiles of sediment in suspension, particularly when estimating the reference concentration.

[35] In Tests 4 and 6 there was clear evidence that a ripple had migrated beneath the ABS transducers by approximately a full wavelength during the course of the observational period. This has allowed the sediment concentration field to be studied, both temporally and spatially, over a full ripple wavelength. While the approach adopted relies on the assumption that the profile shape remained more or less unchanged as the ripple migrated beneath the ABS transducers, this assumption is felt to be reasonably well justified [see *Thorne et al.*, 2002]. Figure 3 shows a sand ripple passing beneath the ABS during the 1024-s recording period during Test 6, the ripple length and height being, respectively, about 0.4 m and 0.06 m. Ten equally spaced, numbered locations are indicated on the ripple shape.

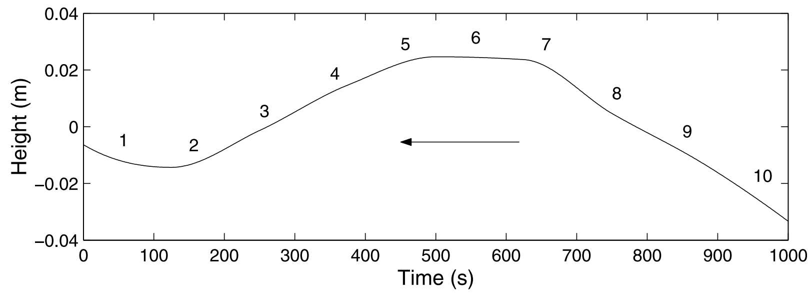


**Figure 3.** Bed location determined by the ABS system during Test 6. Here a ripple migrated by a full wavelength during the 1024-s recording period. Ten successive numbered locations are indicated on the moving profile, the direction of ripple migration being shown by the arrow.

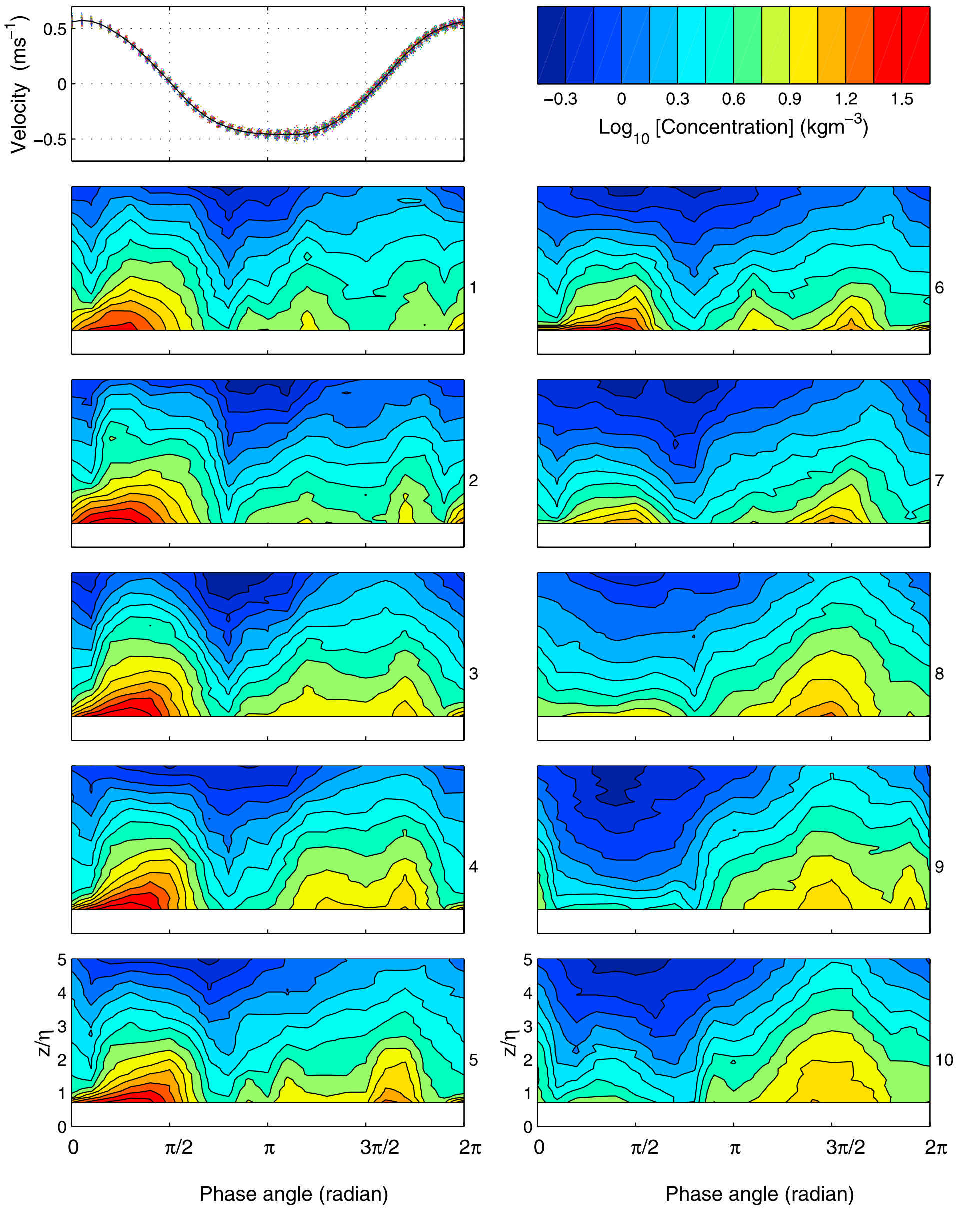


**Figure 4.** Intrawave ECM velocity and suspended ABS concentration results for Test 6. The top left panel shows the measured free-stream velocity for successive wave cycles during the observational period of 1024 s. The ten numbered panels show the intrawave concentrations at the respective positions on the moving bed profile in Figure 2. The ABS results, which were obtained with the 2-MHz transducer, are shown for the bottom 0.3 m of the flow, down to a height of 0.01 m above the ripple crest level. The ABS vertical bin size was 0.01 m. The colors in the contour plots are defined in the color bar as $\log_{10}[c]$ where $c$ is the phase-averaged concentration in kg m$^{-3}$.

[36] In Figure 4, intrawave results are shown for Test 6. Here the top left panel shows the free-stream wave velocity measured by an ECM mounted on STABLE at a height of 0.3 m above the bed. The velocities in successive wave cycles are superimposed in this plot in order to indicate the repeatability of the regular, weakly asymmetrical waves. Peak free-stream velocity may be seen to have occurred shortly after the phase angle defined as 0°.

[37] The remaining panels in Figure 4 show the corresponding intrawave ABS concentrations during the wave cycle at each of the 10 (numbered) locations on the bed shown in Figure 3. The choice of 10 locations corresponded with the acoustic "foot print" on the bed which was of size 0.06, 0.06, and 0.03 m for the 1-, 2-, and 4-MHz transducers, respectively. These results, which are considered to be some of the most detailed and accurate to have yet been produced under full-scale waves for the rippled bed regime, were obtained in vertical bins of height 0.01 m with the 2-MHz ABS transducer. (Similar results were obtained with the two other transducers, but these are not shown for brevity.)

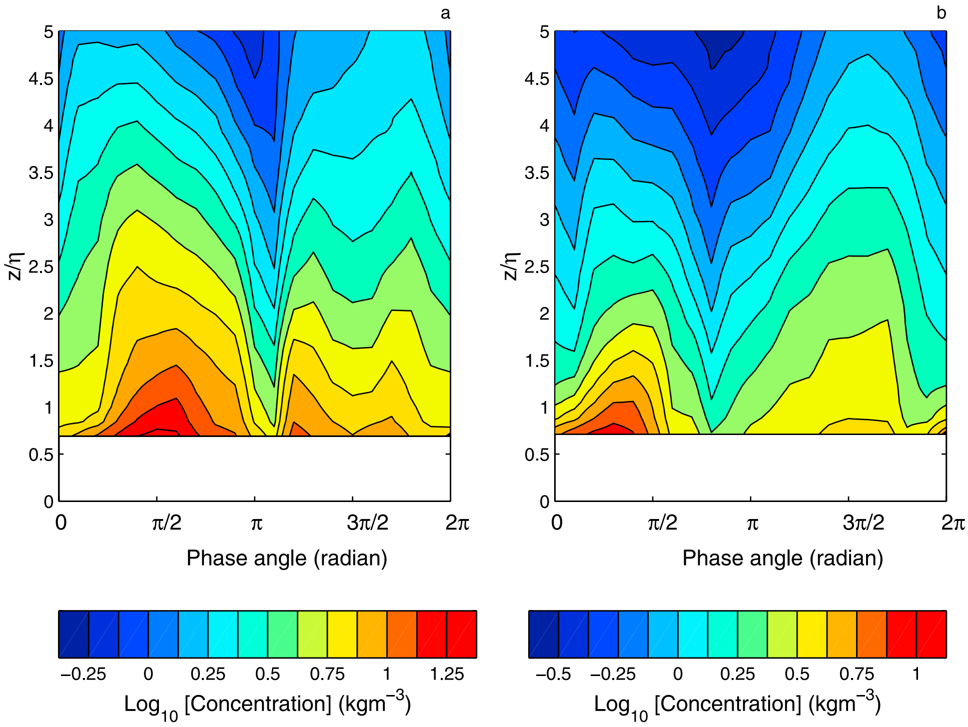


**Figure 5.** Horizontally (ripple) averaged ABS concentrations for (a) Test 4 and (b) Test 6. The results have been obtained by phase averaging the results for the 10 bed locations for the respective tests (shown for Test 6 in Figure 3). This procedure was repeated for each ABS frequency, and the mean of the three outcomes was then taken. The colors in the resulting contour plots are defined in the color bar as $\log_{10}[c]$ where $c$ is the phase-averaged concentration in kg m$^{-3}$.

The concentration results are shown for the bottom 0.25 m of the flow, well below the region of flow possibly influenced by STABLE. Each numbered panel shows the concentration down to a height of 0.01 m above the crest level, and represents a phase average over 20 wave periods when the numbered location was below the ABS transducer. At locations 1 to 5, the relatively high concentrations for phase angles less than about 1.7 rad (or 100°) indicate that sand is being trapped in the growing vortex during the later part of the "positive" wave half cycle. The concentration at these locations then drops sharply following vortex ejection at flow reversal and, although the concentration does exhibit peaks during the succeeding half cycle, these are of significantly smaller magnitude. The fact that there are two distinct peaks in the second half cycle above locations 1 to 5 is probably associated with the passage of sediment-laden vortices ejected from successive upstream ripples. This is a reasonable inference, given the value of $D_1/\lambda \approx 1$ in the present case. At locations 7 to 10 on the opposite ripple face, a similar sequence of events can be observed. However, the high-concentration region that develops here prior to flow reversal extends to a rather greater height than that above the opposite ripple face in the previous half cycle. Also, at locations 7 to 10, there appears to be only one minor concentration peak in the succeeding half cycle. Some difference between the two wave half cycles is to be expected in respect of the concentration field, since not only was the wave weakly asymmetrical, but so also was the bed profile shape migrating below the ABS.

[38] The overall picture that emerges from the 10 panels in Figure 4 is of a coherent phenomenon consistent with the entrainment of sediment in the vortex above the ripple lee slope in each wave half cycle, and the shedding of this sediment-laden vortex at flow reversal. Here we do not attempt to model this complex phenomenon in 2DHV, but instead seek a simple 1DV description. This has been done by phase averaging the results for the 10 bed locations, thereby providing a ripple-averaged description of the height- and time-varying concentration field. A ripple-averaged result was obtained for each of the three ABS frequencies, and the mean of the three measurements was then taken. The outcome is shown in Figure 5 for both Test 6 and Test 4. The ripple-averaged description comprises two concentration peaks per wave cycle, occurring somewhat ahead of flow reversal, and decaying with height above the bed. The fact that the ripple-averaged concentration field is highly coherent, and logically related to the vortex shedding process, acts as a justification for the development of the present simplified 1DV model. Comparisons between the model predictions and the ripple-averaged concentration data are presented in the next section.

[39] Finally, based on the results in Figure 5, Figure 6 shows the wave-cycle-mean, horizontally averaged, ABS-concentration profiles for Tests 4 and 6 measured relative to the ripple crest level, together with the measured pumped-sample values of concentration at six heights above the bed. The agreement between the two profiles illustrates the veracity of the acoustic measurements. Comparisons be-

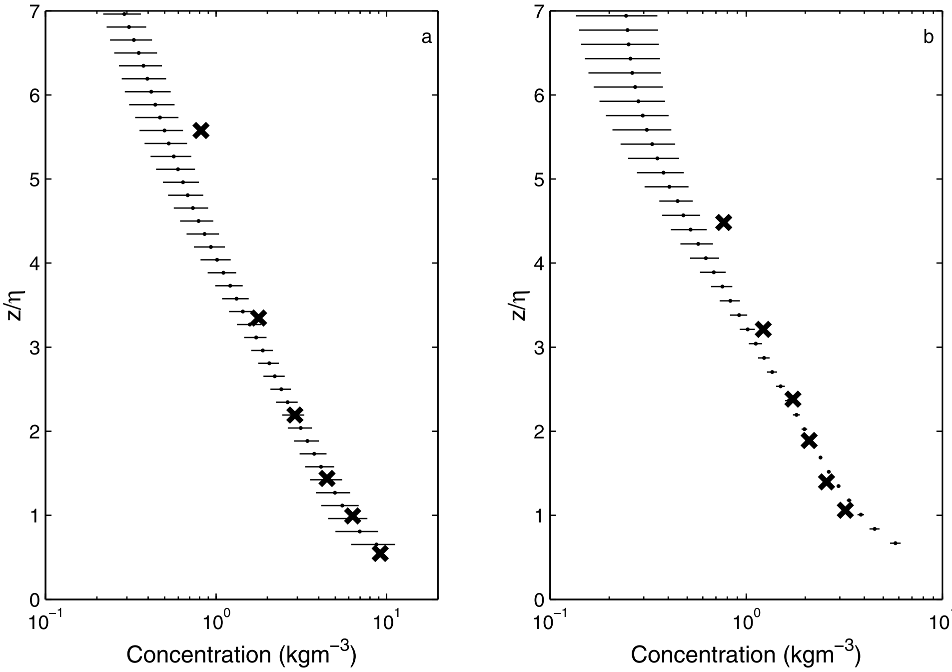


**Figure 6.** Wave-cycle-mean, horizontally averaged, ABS concentration profiles for (a) Test 4 and (b) Test 6, measured relative to the ripple crest level. The ABS results are shown by the dots, around each of which the horizontal bar represents the standard error obtained from the three concentration profiles at the three ABS frequencies. The crosses show the mean concentrations obtained by pumped sampling.

tween the predicted and measured cycle-mean profiles of concentration are also presented later.

## 4. Model Comparisons With Deltaflume

### 4.1. Model Inputs

#### 4.1.1. Near-Bed Velocity Field

[40] It was found by *Thorne et al.* [2002] that if linear wave theory is used to calculate near-bed velocity amplitudes corresponding to the measured wave heights ($H$) and periods ($T$) given in Table 1, the results overestimate the amplitude of the first-harmonic (i.e., fundamental) component measured by the ECMs on STABLE (at heights of 0.30, 0.61, and 0.91 m above the bed) by 9% ± 3%. Although this could have been due in part to the presence of STABLE, it is also the case that since the waves were slightly asymmetric (i.e., weakly steep crested), linear theory may not provide a sufficiently accurate representation of the velocity field. This is an important issue, since uncertainty of 10% in the near-bed velocity amplitude can translate into uncertainty of about 50% in the reference concentration in the present formulation.

[41] In order to provide realistic inputs for the present model runs, a 9% reduction has been applied to the wave heights in Table 1 [following *Thorne et al.*, 2002] and Stokes second-order theory has then been used to provide the near-bed values of $U_1$ and $U_2$ given in Table 2. The resulting near-bed asymmetry parameter $B = U_2/U_1$ may be seen never to exceed 0.066, indicating the presence of only weakly asymmetric waves. Also listed in Table 2 are the corresponding values of the wave Reynolds number and relative roughness.

[42] In order to shed further light on the discrepancy between the predictions of linear theory and the measured wave velocity amplitudes, comparisons have been made (in each case focusing on the amplitude of the first harmonic of the velocity field) involving higher order wave theories. First, Stokes third-order theory, based on the theory of Brink-Kjaer as stated by *Svendsen and Jonsson* [1980] was found to produce a marginal improvement in the results, but only accounting for about 1% of the original discrepancy of 9%. (Relaxation of the mass flux constraint in this theory made no difference to the results in the present cases.) Second, the Stream Function theory of *Dalrymple* [1974] was also used (directly from the web site: http://www.coastal.udel.edu/faculty/rad/index.html). At tenth order this theory accounted for 2–3% (4% in the case of the largest wave) of the overall discrepancy of 9%, possibly confirming the earlier suggestion that STABLE might have

**Table 2.** Derived Parameters for the Deltaflume Experiments[a]

| Test | $U_1$, m s$^{-1}$ | $U_2$, m s$^{-1}$ | $B = U_2/U_1$ | $RE \times 10^{-5}$ | $A_1/k_s$ | $w_s$, mm s$^{-1}$ |
|---|---|---|---|---|---|---|
| 1 | 0.539 | 0.0294 | 0.0545 | 2.3 | 2.3 | 24.9 |
| 2 | 0.541 | 0.0296 | 0.0547 | 2.3 | 2.3 | 25.1 |
| 3 | 0.407 | 0.0167 | 0.0411 | 1.3 | 1.8 | 19.1 |
| 4 | 0.652 | 0.0430 | 0.0659 | 3.4 | 3.0 | 29.2 |
| 5 | 0.525 | 0.0279 | 0.0531 | 2.2 | 2.2 | 24.4 |
| 6 | 0.534 | 0.0288 | 0.0540 | 2.3 | 2.3 | 24.7 |
| 7 | 0.423 | 0.0084 | 0.0199 | 1.1 | 1.7 | 20.7 |
| 8 | 0.340 | 0.0196 | 0.0575 | 1.1 | 1.8 | 15.0 |
| 9 | 0.487 | 0.0240 | 0.0493 | 1.9 | 2.1 | 22.7 |
| 10 | 0.406 | 0.0167 | 0.0411 | 1.3 | 1.8 | 19.1 |

[a]Near-bed velocity amplitude (first harmonic ($U_1$), second harmonic ($U_2$)); asymmetry parameter ($B$), Reynolds number ($RE$), relative roughness ($A_1/k_s$) and settling velocity ($w_s$).

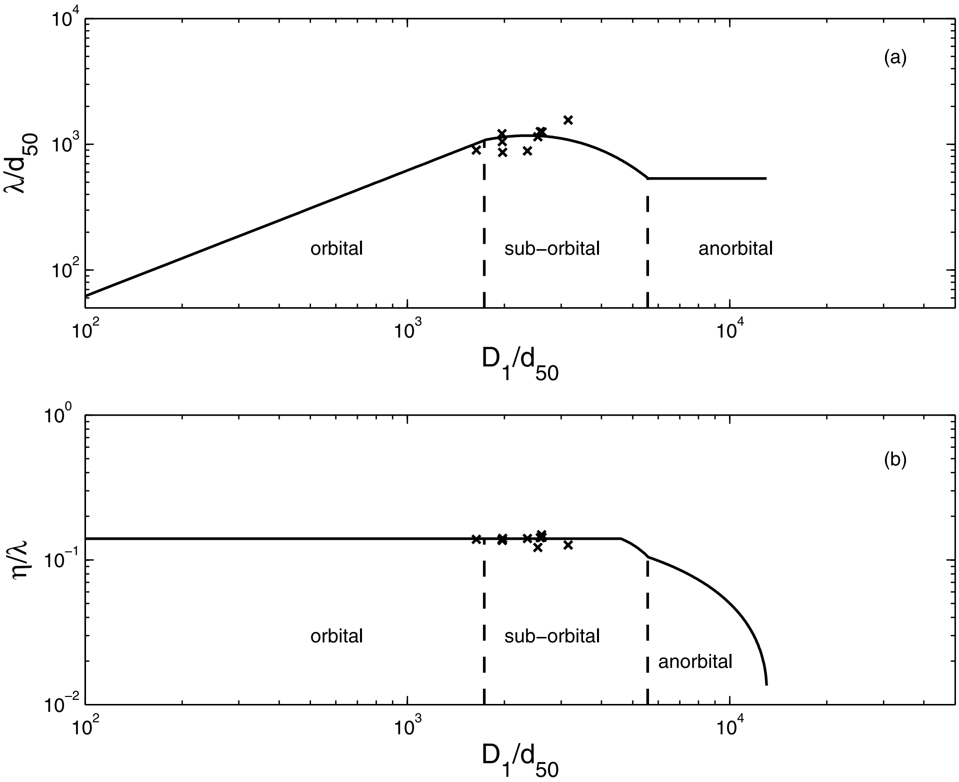


**Figure 7.** Normalized ripple dimensions: measured (crosses), and predicted (line) using a modified version of *Wiberg and Harris*' [1994] formulation. (a) Wavelength (λ) versus orbital diameter ($D_1$), normalized in each case by the median grain diameter ($d_{50}$); (b) ripple steepness (η/λ) versus normalized orbital diameter.

had some effect on the near-bed velocity field. Even taking into account the stated accuracy of the surface-following wave gauges in the Deltaflume (±25 mm, i.e., about 2.5% of the wave amplitude) and of the ECM's (±2 mm/s, i.e., about 0.5% of the measured velocity amplitude), the discrepancy cannot be accounted for fully.

#### 4.1.2. Ripple Dimensions

[43] Unless the measured ripple dimensions are imposed as inputs, the model estimates η and λ using the formulation for waves alone of *Wiberg and Harris* [1994]. Figure 7 shows that the ripples in almost all of the Deltaflume tests were in the central "suborbital" range. Here, in order to provide the model with a reasonable overall representation of the ripple dimensions, *Wiberg and Harris*' [1994] formulation was modified in the orbital and suborbital regimes by the imposition of a maximum value of ripple steepness of 0.14 (in place of the standard value of 0.17). The resulting ripple dimensions, which exhibit some departure from the measured values in individual cases, have been used in the prediction of the bed roughness $k_s$ (equation (9)) and also the cycle-mean, reference concentration $C_0$ at the ripple crest level (equation (18)).

#### 4.1.3. Reference Concentration

[44] On the basis of the calculated ripple dimensions, the reference concentration $C_0$ has been determined from equation (18). As noted earlier, for the present Deltaflume data, *Thorne et al.* [2002] found that *Nielsen*'s [1986] empirical constant (=0.005) in this equation should be reduced to the value 0.0022. The effect of this change can be seen in Figure 8 where the predicted values of $C_0$ (full line) are compared with the measured mean values (extrapolated to the ripple crest level using the ABS profiles). Evidently, in individual cases, there is significant uncertainty in the value of $C_0$ due to the $\theta_r^3$ dependency in equation (18), but the general behavior of $C_0$ is quite well represented by Nielsen's cubic relationship. The need for the reduced constant is probably related to the relatively small proportion (10–40% by volume in the respective tests) of the bed material that was entrained into suspension (see section 4.1.4). The present model takes no account of grain-mixture effects such as bed armoring, other than by the above, rather ad hoc, adjustment of the empirical constant in equation (18).

#### 4.1.4. Settling Velocity of the Grains in Suspension

[45] A necessary step in the computation concerns the determination of the suspended sediment grain size ($d_s$) and hence the settling velocity ($w_s$). The procedure used was described earlier, and Figure 9 shows a typical example of the results for Test 6. Here the measured cumulative grain size distribution of the bed sediment is shown, together with its representation by a lognormal distribution. This is based on the median grain diameter $d_{50}$ = 0.329 mm, together with an optimized value of the geometric standard deviation $\sigma_g = [d_{84}/d_{16}]^{1/2}$ = 1.55 that gives a good representation of the finer 50% of the bed sediment. (A different value of $\sigma_g$ would be required for a good description of the coarser 50%; see *Li and Davies* [2001] for details of the method.)

[46] The same value of the Shields parameter (θ′, skin friction) on a flat bed has been used here as for the

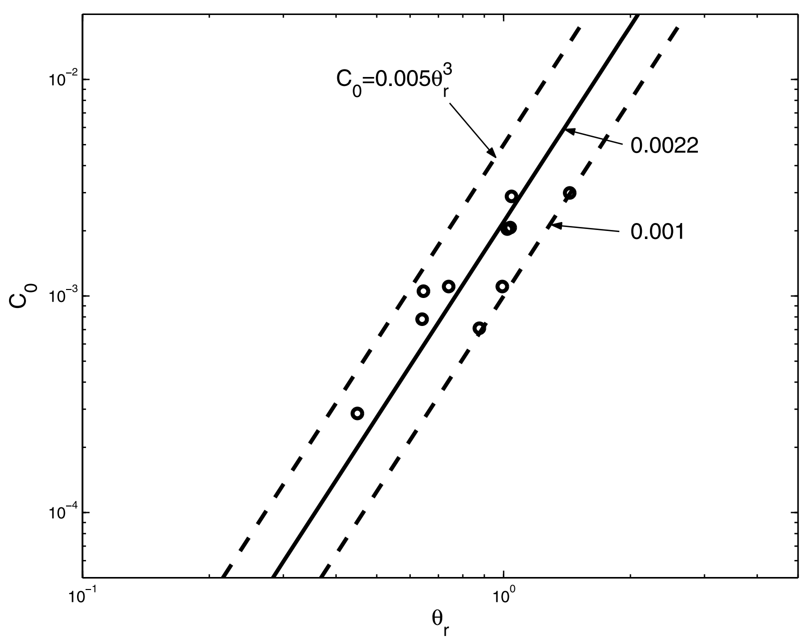


**Figure 8.** Cycle-mean reference concentration at the crest level ($C_0$) inferred from the measured ABS concentration profiles (○). The ripple- adjusted Shields parameter ($\theta_r$) is based on equations (19) and (20) in which predicted values have been used for ripple height ($\eta$) and length ($\lambda$). The full line corresponds to equation (18), and the dashed lines correspond to the same equation but with different constants of proportionality.

calculation of the reference concentration; for Test 6, $\theta' = 0.320$. On the basis of the criterion of *Fredsøe and Deigaard* [1992] (stated earlier) the largest grains capable of being lifted into suspension correspond in Test 6 to $d_{crit} = 0.257$ mm ($\approx d_{29}$), which is far smaller than the median diameter of the bed material. Next, assuming a single grain size in suspension, the median diameter of these grains has been determined from the assumed log normal curve as $d_s = 0.206$ mm ($\approx d_{14.5}$). Finally, on the basis of the formula of *Soulsby* [1997], the settling velocity has been determined as $w_s = 24.7$ mm s$^{-1}$. The way in which this approach may be extended to multiple grain sizes in suspension has been explained by *Davies and Thorne* [2002]. There it is shown (for Test 3) that use of multiple grain sizes produces a

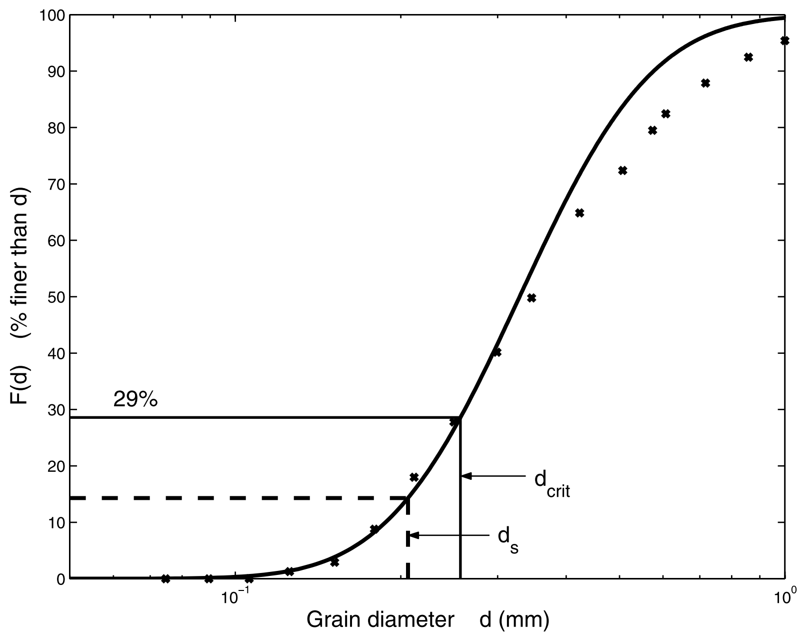


**Figure 9.** Cumulative grain size distribution of the bottom sediment (crosses) and its representation by a lognormal distribution curve (thick line). Also shown, for Test 6, is the diameter ($d_{crit}$) of the largest grains in suspension, and the median diameter ($d_s$) of the suspended sediment.

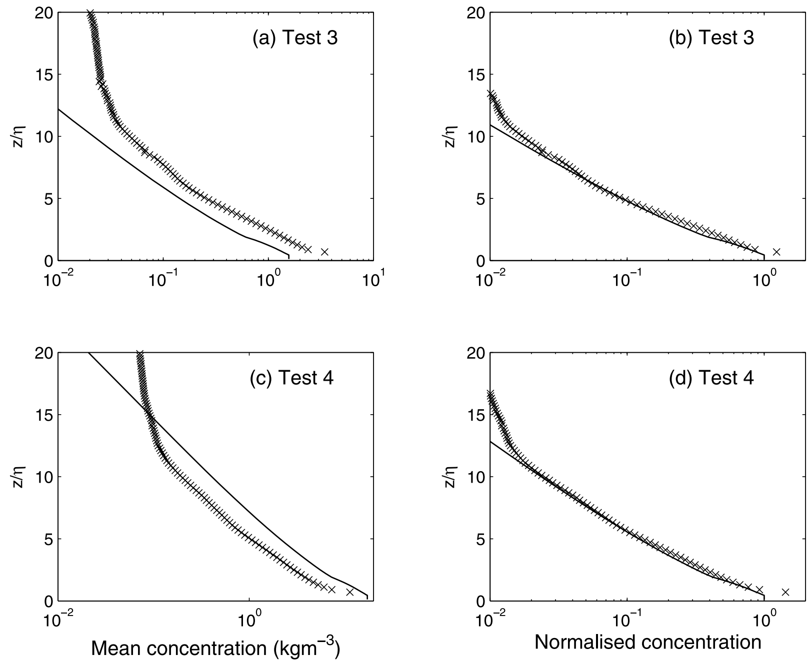


**Figure 10.** Horizontally averaged time-mean concentration profiles for Tests 3 and 4: (a, c) absolute concentrations, (b, d) concentrations normalized by the reference concentration at the ripple crest level. The ABS data is represented by the crosses in bins of height 0.01 m.

significant modification to the mean concentration profile and, more importantly, a very good prediction of $d_s$ and its variation with height above the bed. For simplicity in what follows, the computations have been restricted to a single grain size in suspension in the respective tests.

### 4.2. Results

[47] Typical time-mean, horizontally averaged, concentration profiles are shown in Figure 10 for Tests 3 (top) and 4 (bottom). (Further mean profiles have been presented by *Davies and Thorne* [2002].) The predicted settling velocities ($w_s$) of the grains in suspension in the respective tests were 29.2 and 19.1 mm s$^{-1}$, corresponding to $d_s$ = 0.230 mm and 0.175 mm. In the case of Test 4, 42% (by volume) of the bed material was able to be entrained into suspension, compared with 15% in the case of Test 3. The model profiles are shown both as absolute concentrations and also as relative concentrations, normalized by the reference concentration $C_0$. The predictions show good overall agreement with the data in the lower vortex-dominated layer (of thickness about 2$\eta$), and also in the outer turbulent layer above this. However, in these and most other tests, systematic differences occur above a height of $z \approx 10\eta$. As noted earlier, some variation is expected between tests on account of the uncertainty in the predicted value of $C_0$ in individual cases. In contrast, the slope of the mean concentration profiles in the lower layer has been optimized through the choice of the factor $\beta$ (= 4.0) relating the cycle-mean diffusion coefficients of sediment ($\overline{K}_s$) and momentum ($\overline{K}$), yielding good agreement in respect of the slope in all cases.

[48] In Figure 11 the nature of the intrawave model solution is presented for Test 4. The panels show profiles of (Figure 11a) velocity at 20 equally spaced phase angles though the wave cycle, and (Figure 11b) volumetric concentration and (Figure 11c) eddy viscosity, each at 11 phase angles though the half wave cycle from 0 to $\pi$. (Figure 11d is discussed below.) The profile highlighted by the thicker line in each subplot corresponds to the phase angle $\pi/2$ just after free-stream flow reversal. The various profiles are shown with respect to the mean bed level ($z$ = 0). The velocity profiles, which are plotted from height $z = k_s/30$ at which $\langle u_p \rangle = 0$, exhibit phase shifts in the near-bed layer, and also some asymmetry as expected for weakly asymmetric waves; for example, there is a somewhat greater overshoot in velocity, at a height of about $z/\eta = 1$ (predicted $\eta$ = 0.05 m), beneath the wave crest than beneath the trough. The oscillatory boundary layer is contained mainly within a layer of thickness just less than two ripple heights above the mean bed level. The suspended concentration decreases rapidly with height in this layer, and the concentration profiles also exhibit phase shifts. Below the ripple crest level at $z/\eta = {}^1\!/_2$, the concentration is not modeled and is simply shown (by the vertical lines) as taking the instantaneous crest value. The corresponding profiles of the eddy viscosity $K$ in the lower vortex layer ($z/\eta \leq 2$) are prescribed on the basis of equation (10). These profiles are strongly time varying and constant with height. As noted earlier, $K$ is constrained to remain positive throughout the wave cycle. At the matching level ($z/\eta = 2$) between the lower (vortex) and upper layers, the profiles of $K$ connect continuously with profiles derived using the t.k.e. closure scheme. Above $z/\eta \approx 4$, the time variation in $K$ becomes far smaller than the mean value of $K$, which has a parabolic behavior. It may be noted that both the velocity and concentration profiles undergo an equivalent matching at $z/\eta = 2$, though this is not so apparent due to the smoother nature of the curves at these heights. It would have been

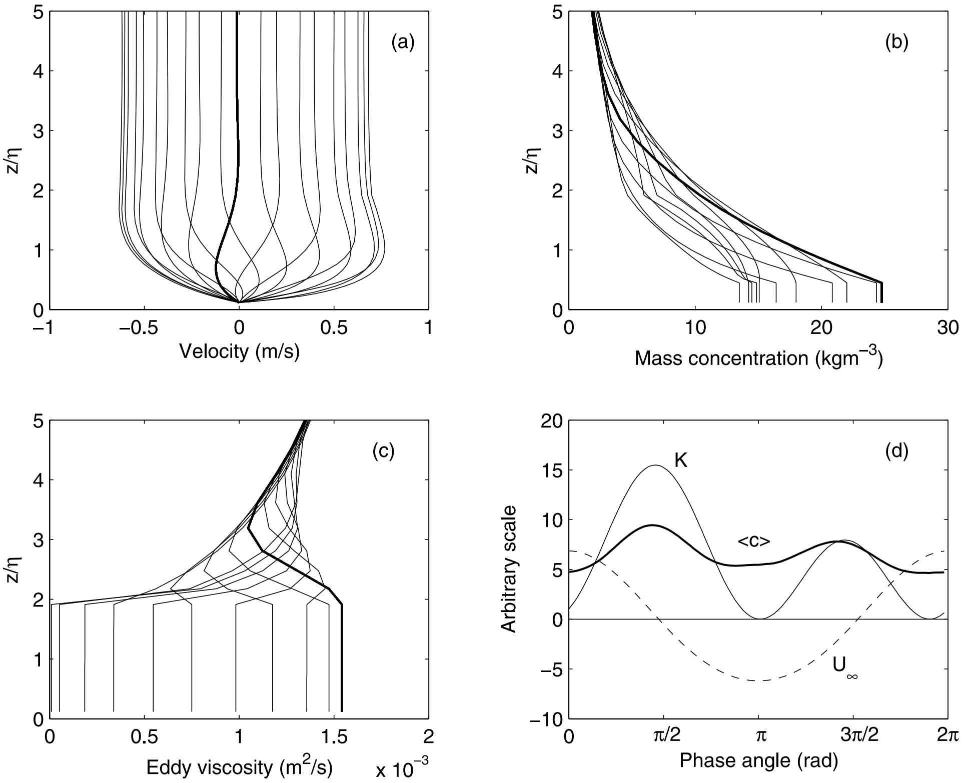


**Figure 11.** Intrawave model results for Test 4. Instantaneous profiles of (a) ripple-averaged velocity (0 to $2\pi$), (b) concentration (0 to $\pi$), and (c) eddy viscosity (0 to $\pi$); (d) time variation of free-stream velocity ($U_\infty$), eddy viscosity ($K$) in the lower vortex layer, and concentration ($\langle c \rangle$) at the ripple crest level, each on an arbitrary vertical scale. The profile highlighted by the thick line in Figures 11a–11c corresponds to the phase angle $\pi/2$.

possible to "connect" the $K$-profiles more smoothly at height $z/\eta = 2$. However, this was not done since the numerical solution was sufficiently well behaved around the matching level.

[49] In order to highlight the phase relationship between these three key physical variables, Figure 11d shows time series of free-stream velocity, eddy viscosity in the lower vortex layer, and concentration at the ripple crest level (each on an arbitrary vertical scale). The free-stream velocity exhibits slight asymmetry beneath the crest ($\omega t = 0$) and trough ($\omega t = \pi$). Peak eddy viscosity occurs 0.07 rad (or 4°) in advance of free-stream flow reversal following the passage of the crest, and has a second, smaller, peak value just in advance of flow reversal following the passage of the trough. The ripple-averaged concentration at the crest level is also asymmetrical in respect of the passage of the wave crest and trough. Owing to the assumed phase of the time-varying sediment pick-up function, the peak in concentration following the passage of the crest occurs at the time of peak eddy viscosity in the lower vortex layer, i.e., just ahead of flow reversal. This assumption is probably reasonable, in general, but not precise in individual cases, as discussed in relation to Figures 14 and 15 later.

[50] In Figures 12 to 15 the predicted and measured, ripple-averaged, time-mean and intrawave, suspended concentration fields are compared for Tests 4 and 6 for which a ripple migrated by a full wavelength during the test. (It should be noted that the "measured" data here comprise the concentration field averaged over the three ABS transducers.) Figure 12 shows a contour plot for Test 6 of the predicted sediment concentration field from the crest level ($z/\eta = 1/2$) up to a height of $z/\eta \approx 5$, together with the free-stream oscillation. The peak near-bed concentration occurs just ahead of flow reversal following the passage of the wave crest at $\omega t = 1.497$ (or 85.8°), and then decays with height, suffering a phase lag as it does so. The concentration peak just ahead of the second flow reversal following the trough at $\omega t = 4.786$ (or 274.2°), which is somewhat less pronounced, suffers the same attenuation and phase lag with increasing height. The matching level ($z/\eta = 2$) is evident in this plot through some minor irregularity in the contours. However, the solution is generally well behaved at the matching level. The model solution in Figure 12 resembles quite closely the observed concentration field shown for Test 6 in Figure 5b. The timing of the two observed concentration peaks during the wave cycle is represented convincingly at the bed level, and the attenuation and phase lagging of these peaks with increasing height is also evident. Moreover, the measured asymmetry in the strengths of the concentration peaks in the two wave half cycles is represented by the model, at least qualitatively.

[51] Figure 13 shows, for Test 4, time series of measured and predicted (normalized) concentration at four heights above the ripple crest level. The first two heights (Figures 13a and 13b) correspond to the lower layer of the model, the third height (Figure 13c) lies fairly close to

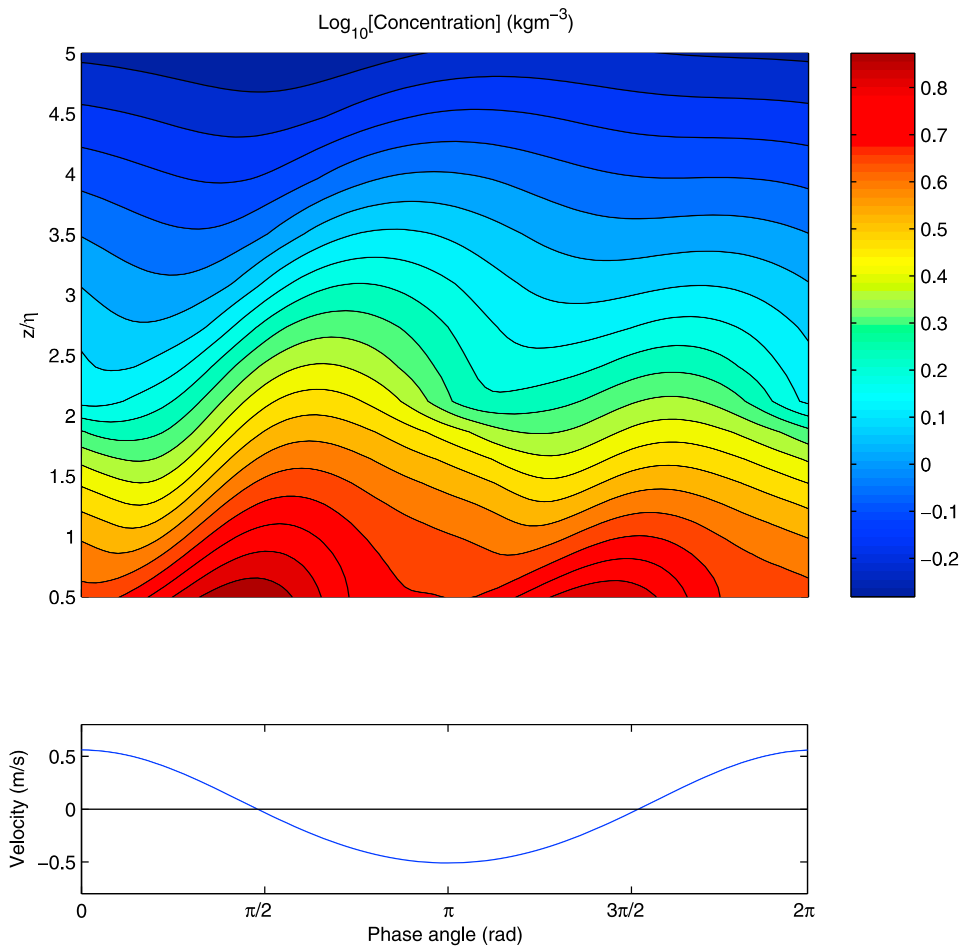


**Figure 12.** Contours of intrawave suspended concentration in the bottom 0.3 m predicted for Test 6, together with the free-stream velocity.

the matching level, while the fourth height (Figure 13d) lies in the outer layer. In the lower layer, the model reproduces the phase angle of the observed concentration peaks quite convincingly (taking account of the fact that the concentration variation in the second half-cycle is double peaked). However, it underestimates both the magnitude of the symmetrical contribution to the time variation in concentration and the unequal magnitudes of the respective concentration peaks. It would appear from this that the assumed sediment pick-up function (equation (17)) produces insufficient time variation in the pick-up rate. The fact that there is an underestimate in the asymmetry in concentration between the peaks is less surprising since, as noted earlier, equation (17) contains no asymmetry contribution in respect of the assumed concentration gradient at the crest level. This forces any asymmetry in the model solution to be relatively small, and probably leads, in turn, to an underestimate in the magnitude of the predicted wave-related component of the net sand transport rate (see section 5). Finally, Figure 13 confirms that, in the outer layer, the measured and predicted concentrations are relatively small. Here the behavior of the observed time series in concentration is represented quite well by the model, but subject to a substantial phase shift between the two time series. Nevertheless, despite various detailed points of disagreement, the time series comparison in Figure 13 provides general support for the 1DV modeling approach.

[52] As a more exacting comparison, both the measurements and the model solutions have been harmonically analyzed for Tests 4 and 6 with results that are shown in Figures 14 and 15, respectively. In the discussion of these results, attention is focused mainly on the mean and second harmonic components of the concentration field, since the present modeling effort was directed primarily at the prediction of these two components, not least through the formulation of the pick-up function (equation (17)). The second harmonic component describes the two concentration peaks occurring during the wave cycle. The results are expressed in the form

$$\frac{\langle c \rangle}{C_0} = \frac{C}{C_0} + \frac{C_2}{C_0} e^{i(2\omega t + \varphi_{2c})}, \qquad (22)$$

where $C$ and $C_2$ are, respectively, the mean component of ripple-averaged concentration, and the amplitude of the second harmonic component of concentration, with each term normalized by the (measured or predicted) reference concentration $C_0$. As expected, the profiles of $C/C_0$ for both tests (Figures 14a and 15a) are predicted quite well, since the coefficient $\beta$ was chosen with this end in mind. It may

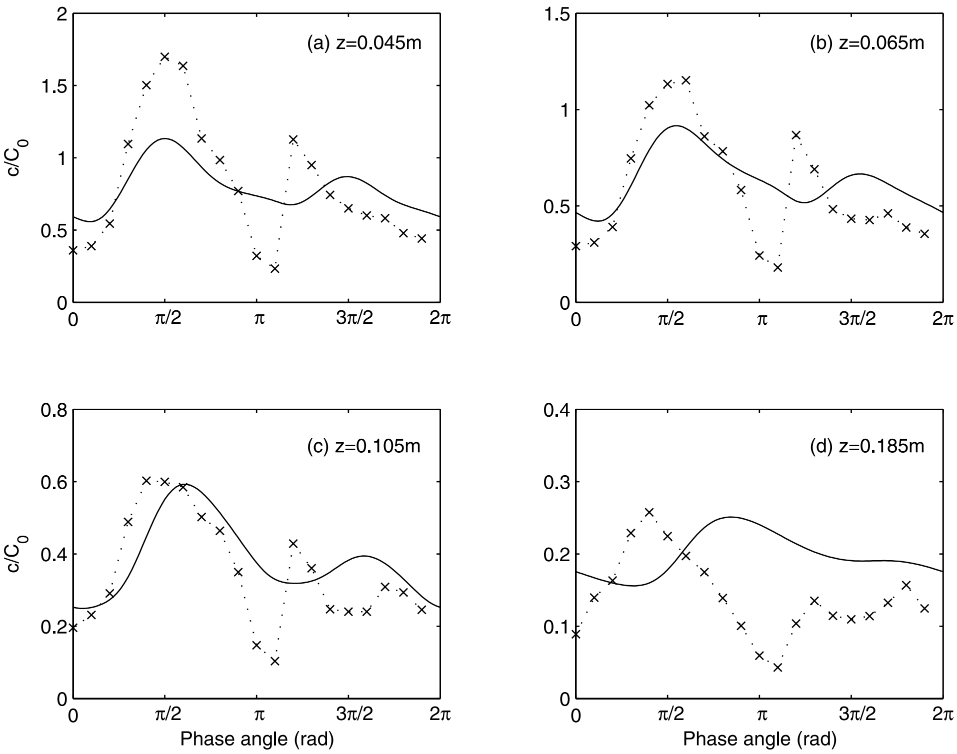


**Figure 13.** Comparison for Test 4 between ripple-averaged time series of predicted (solid line) and ABS measured (crosses, dotted line) concentration at four heights above the ripple crest level: $z$ = (a) 0.045, (b) 0.065, (c) 0.105, and (d) 0.185 m.

be noted that the lowest ABS measurement level was excluded from the calculation of the (measured) reference concentration $C_0$. Also, as in Figure 11, the model results below the crest level are shown simply as vertical lines.

[53] The magnitude of the second harmonic component $C_2/C_0$ is underpredicted by a factor of about 2 for both tests (Figures 14b and 15b). The two layer structure of the model is clearly evident in these figures, with conditions in the outer layer being fairly well predicted. The underprediction of $C_2/C_0$ in the lower layer may seem surprising in view of the strongly time-varying nature of the sediment pick-up function (equation (17)). The results of the present harmonic analysis confirm the point made in the discussion of the time series in Figure 13 and suggest that an even more strongly time-varying, non-negative, pick-up function might have been appropriate for the simulation of the present tests.

[54] As far as the phase angle of the second harmonic component is concerned, it is here that the qualitatively different nature of the new modeling approach is apparent. Essentially, peak concentration occurs at around the time of flow reversal in both model and experiment. The harmonic analysis of the ABS data for Test 6 (Figure 15c) reveals that peak, ripple-averaged concentration at the lowest measurement level occurs ahead of flow reversal by 0.86 rad (or 49°). In successive 0.01-m-height bins above this, the concentration peak is then phase lagged, coinciding with free-stream flow reversal (defined including the asymmetry effect) at a height of $z/\eta = 5.2$. It should be noted that there was some uncertainty in the synchronization of the velocity and ABS logging systems, believed to be equivalent to ±0.157 rad (or ±9°) of phase (corresponding to the ABS digitization interval of 0.314 rad or 18°, i.e., 4-Hz sampling of the sediment profiles during the 5-s wave period). This uncertainty is represented by the two solid lines drawn parallel to the calculated phase profile. The harmonic analysis of the data for Test 4 (Figure 14c) shows generally similar behavior to Test 6, but with some notable differences. First, the peak concentration measured just above the crest occurred closer to flow reversal than in Test 6 and, secondly, after experiencing a small phase lag in the near-bed layer, no further lag then occurred (a slight phase lead actually becoming discernable). The model shows the same general behavior as the data in the lower layer, in that there is a progressive lag in phase with increasing height above the bed (though with a minor reversal of this trend in the outer part of the lower layer between $z/\eta = 1.6$ and 2.0). In Test 4 the phase of the concentration peak is predicted rather well in the lower layer; in Test 6, however, the observed peak occurred earlier than in the model solution.

[55] It may be recalled that sediment pick-up at the crest level is constrained (through the choice of $\varphi_c$ in equation (17)) such that peak concentration occurs just ahead of flow reversal. In the present tests (which have not been subject to individual tuning), this constraint is evidently too simplistic, forcing peak concentration in the solution to occur somewhat later than observed, at least in the case of Test 6. In the lower layer (up to height $z/\eta \approx 2$), the predicted change in phase lag with height is fairly similar to that observed, especially in the case of Test 6. However, close to the crest level itself, the model predicts a rather more rapid phase change than that observed. This may be attributable to the fact that, as noted in section 2, the

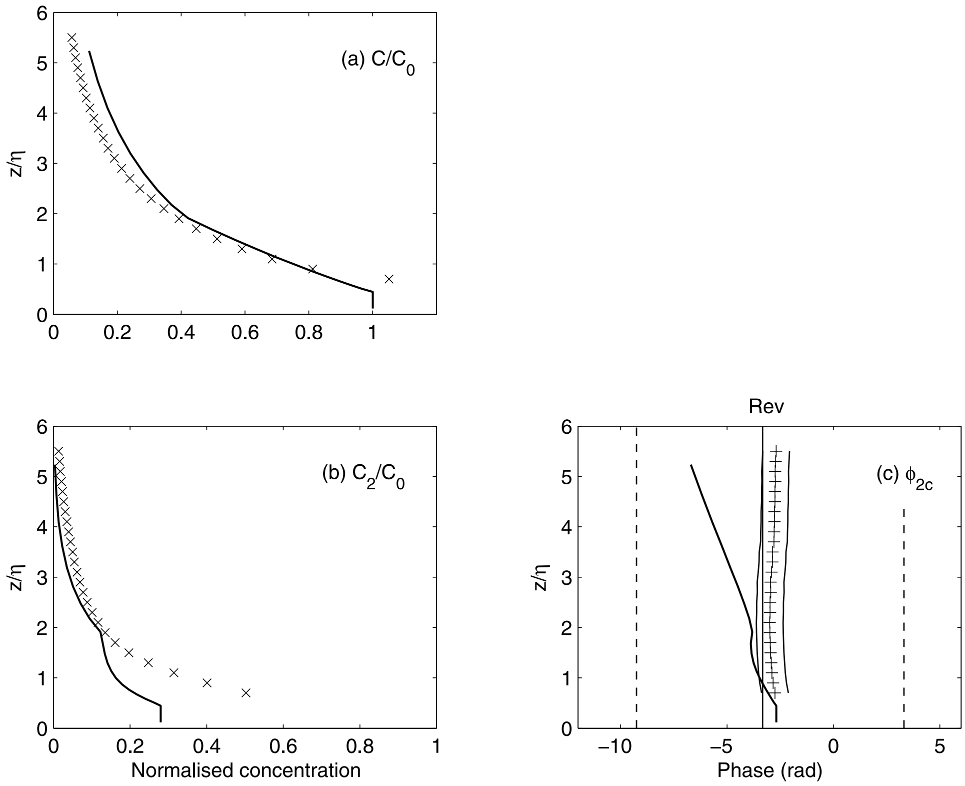


**Figure 14.** Vertical profiles of the harmonic components of the measured and predicted suspended sediment concentration fields for Test 4. The results are expressed in the form of equation (22). The model results are shown by thick solid curves, and the data are shown by symbols (magnitude, crosses; phase, pluses). The magnitudes of (a) the mean and (b) second harmonic components of concentration are normalized by the reference concentration at the crest level. (c) The phases of the second harmonic component are shown in relation to the instant of flow reversal in the free stream following the passage of the wave crest (full vertical line labeled "Rev"). The dashed vertical lines represent the phase angles of the preceding and succeeding flow reversals in the free stream. The full lines parallel to the measured phases represent the uncertainty in the experimental determination of phase angle.

time variation in near-bed eddy viscosity $K$ inferred from the results of the discrete-vortex model of *Malarkey and Davies* [2004] is such that peak $K$ occurs later at the crest level than in the outer part of the vortex layer. Inclusion of this phase behavior in the 1DV model would have the effect of decreasing the rate of change of phase angle with height above the crest, bringing the model into closer agreement with the observations. However, at the present stage of this research, this has been considered to be a refinement too far.

[56] In the outer turbulent layer, represented in the present model by a standard t.k.e. closure scheme, the results for the second harmonic (Figures 14c and 15c) suggest that phase changes in eddy viscosity occur far too rapidly with increasing height compared with the data due, apparently, to the purely diffusive nature of the model in this region. It may be inferred from the data that the rather slower observed changes in phase angle in the outer layer ($z/\eta > 2$) are indicative of the persistence of convection effects associated with vortex shedding. This suggests, in turn, that the matching level between the two layers (at $z/\eta = 2$) may have been underestimated somewhat. It is interesting to note that the lower vortex layer in *Van Rijn*'s [1993] formulation extends to a height of $z/\eta = 3$ above the bed. This point requires further study.

[57] In summary, the results in Figures 14 and 15 suggest that intrawave suspension processes are generally well represented by the present model. The phase of the second harmonic confirms the presence of a peak in sediment concentration just before flow reversal in the free stream. This peak suffers a phase lag with height, though the predicted change of phase with height is greater than that observed. Moreover, the magnitude of the second harmonic is underpredicted, suggesting the need for relatively greater time variation in the assumed pick-up function (equation (17)). Nevertheless, despite some limitations, the existing simple model does succeed in capturing, for the first time in a 1DV formulation, many of the key features of the suspension phenomenon above vortex ripples. Further work is still needed, however, particularly in relation to the accurate prediction of the asymmetry in the magnitudes of the peaks in concentration in the two wave half cycles.

## 5. Discussion

### 5.1. Sediment Fluxes

[58] From the point of view of practical sand transport modeling, it is relevant to consider the importance of the vortex shedding process for net transport above rippled

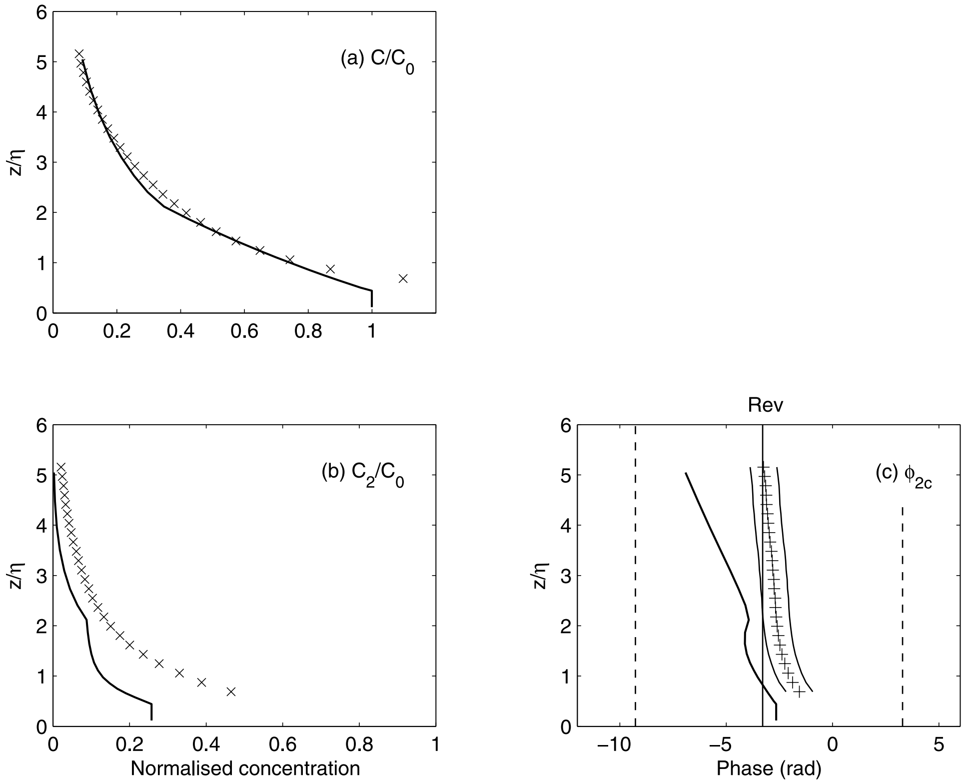


**Figure 15.** Caption as for Figure 14, but here for Test 6.

beds. *Davies and Villaret* [2002] presented comparisons with suspended sediment concentration data obtained in combined wave-current conditions, and showed that the present modeling approach produces improved predictions of the suspended concentration field compared with a classical plane-bed approach in which the bed roughness $k_s$ is simply enhanced to represent the ripples. Here, in connection with the Deltaflume tests, we consider the predicted net transport rate for weakly asymmetric waves alone.

[59] The model predictions for the net sand transport rate are shown for Test 4 in Figure 16, where a distinction is made between the wave-related and current-related components of the suspended load transport. The wave-related component, which is expected to be dominant beneath asymmetric waves above rippled beds, arises in a 1DV model as follows. If the instantaneous (phase ensemble) horizontal velocity $u = u(z, t)$ and concentration $c = c(z, t)$ are expressed as the sum of mean and periodic (or wave) contributions, as follows:

$$u = U + u_w \qquad and \qquad c = C + c_w, \tag{23}$$

where $U = \overline{u}$ and $C = \overline{c}$ (the overbar denoting a time average over an integral number of wave cycles), then the mean (volumetric) transport rate, at height $z$, per width of flow is given by

$$\overline{uc} = UC + \overline{u_w c_w}, \tag{24}$$

where the terms on the right-hand side are, respectively, the current-related and wave-related components of the suspended load transport rate. (Although angle brackets, and subscript $p$ (see equation (1)), have not been included for simplicity, each of the quantities in equations (23) and (24) may be assumed to be both phase ensemble and ripple averaged.)

[60] Figure 16a shows the predicted profile of cycle-mean velocity induced by the weakly asymmetrical waves in Test 4. The mean velocity profile exhibits a forward (“onshore”) jet in the lower part of the wave boundary layer, a reversal in the direction of mean flow within the boundary layer, and a backward (“offshore”) mean flow at the edge of the boundary layer. Although offshore flow at the edge of the boundary layer above very rough and rippled beds is sometimes attributed erroneously to “undertow,” it is actually driven by the mechanics of the bottom oscillatory boundary layer, as demonstrated experimentally by *Mathisen and Madsen* [1996b]. In the case of Test 4, the thickness of the boundary layer was shown earlier (Figure 11a) to be equal to about 2η. The vertical structure of the residual flow shown in Figure 16 has been observed in various laboratory experiments involving regular waves above rippled and very rough beds [*Davies and Villaret*, 1999]. Further, for rippled beds beneath irregular waves, *Chung and Van Rijn* [2003] have presented measured mean velocity profiles most of which show the same mean flow structure, namely an onshore near-bed jet beneath an offshore residual in the outer part of the boundary layer. This velocity structure was examined in detail by *Davies and Villaret* [1999], whose eddy viscosity model, for the rippled and very rough bed regime, has been incorporated (in a slightly modified form) as the lower layer of the present two-layer model. It should be noted that the present

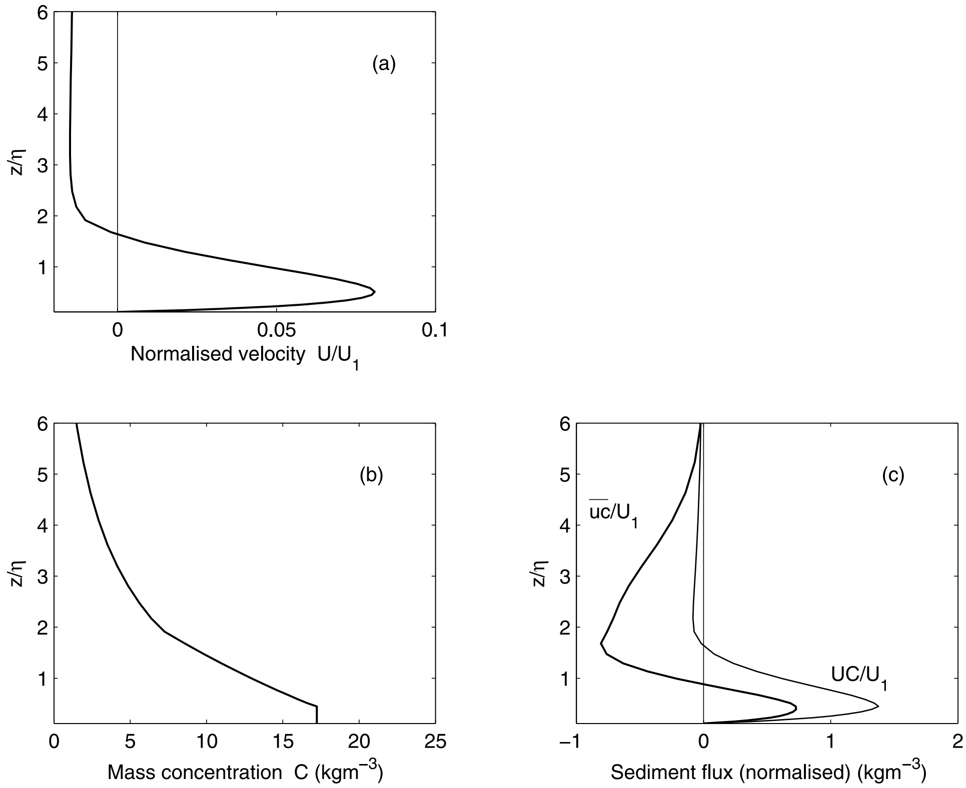


**Figure 16.** Vertical profiles of predicted, ripple-, and time-averaged (a) normalized velocity, (b) suspended concentration, and (c) current-related suspended sediment flux (normalized by $U_1$) $UC/U_1$, and true (current- and wave-related) flux $\overline{uc}/U_1$, for Test 4.

model differs from that of *Davies and Villaret* [1999] in that it does not include "streaming" associated with vertical wave velocities. Therefore the residual velocity profile in Figure 16a should be compared only with the "asymmetry" terms in Davies and Villaret's more general solution. The counterpart of this residual velocity above a flat rough bed was discussed by *Davies and Li* [1997], who showed that beneath asymmetrical waves, the residual velocity is in the offshore direction at all heights through the boundary layer. Again, their analysis did not include "streaming" (which produces an opposing residual current in the onshore direction). In practice, the neglect of streaming will have had a relatively minor effect on the sediment flux profiles discussed below; although the analysis of *Davies and Villaret* [1999] shows that streaming is an important (though not dominant) influence at the edge of the boundary layer, its relative importance diminishes towards the bed, falling typically to O(10%) of the velocity in the residual jet in Figure 16a.

[61] The mean concentration profile in suspension is shown for Test 4 in Figure 16b, wherein constant mean concentration has been assumed between the mean bed level ($z = 0$) and the ripple crest level ($z = {}^1\!/_2\eta$). The product at each height of the mean concentration and associated velocity ($UC$) yields the current-related component of the net transport (Figure 16c). The vertical profile of the current-related transport is dominated by transport in the onshore near-bed jet. However, above a height of about 1.2η above the crest, the net transport is offshore, decreasing toward zero above a height of about 5η. The profile of suspended sediment flux ($\overline{uc}$), including intrawave processes through the modeled wave-related component of the transport, is also shown in Figure 16c. The near-bed onshore jet is still evident in this profile, but the associated transport is greatly reduced in magnitude. In contrast, offshore net transport is now dominant, with maximum flux in the offshore direction occurring within the boundary layer at a height of about 1.2η above the crest. In the case of Test 4, the magnitude of the depth-integrated wave-related transport is about 8 times larger than the magnitude of the current-related transport, and it is in the opposite ("offshore") direction. *Trouw et al.* [2000] presented net transport profiles of the present kind, showing a reversal in the direction of the net transport, based on analysis of results of a 2DHV $k$-ε model. The total net sediment transport rate comprises both suspended load and bed load. The bed load contribution may be considered to comprise mainly the transport associated with the migration of the ripples in the onshore direction. The present Deltaflume experiments were not set up to determine systematically the bed load transport rates arising from ripple migration. This remains a topic for future study.

[62] The flux profiles discussed above were obtained for a single grain size in suspension. Had a multiple grain-size approach been adopted, it may readily be inferred from the profile of $\overline{uc}$ in Figure 16c that coarser grains would be trapped in the near-bed jet and would thus tend to migrate onshore; in contrast, finer grains would be present throughout the boundary layer and would tend to migrate offshore. Thus the present modeling approach, when used with

graded sediment sizes, would give rise to sediment sorting, with coarser grains tending to travel in the direction of wave propagation, and finer grains tending to travel in the opposite direction, as found, for example, beneath shoaling waves on beaches. Those coarser grains that are unable to be entrained into suspension will tend to migrate in the onshore direction as part of the process of ripple migration.

[63] It should be emphasized that the present discussion of net fluxes is based on the model solution only, since no direct measurements of sand transport rates were made during the Deltaflume tests. Also, it may be recalled that the sediment pick-up formulation (equation (17)) used in obtaining the results in Figure 16 was symmetric in respect of the assumed concentration gradient in the two halves of the wave cycle, the only asymmetry in the pick-up function being introduced through the time-varying eddy viscosity. Had some additional asymmetry been introduced into the pick-up function, via the assumed concentration gradient, to represent the likely enhancement of pick-up following the passage of the wave crest, and rather smaller pick-up following the trough, the ratio between the offshore wave- and onshore current-related components of the depth-integrated net transport would, in the case of Test 4, have exceeded 8:1, possibly by a substantial amount. Quantification of this ratio represents an important goal for future research, since these processes are not presently included in coastal sand transport and morphological models. The uncertain predictions sometimes made by these models may be due, in part, to their oversimplistic treatment of local sand transport processes. Some means of parameterizing these processes is needed for use in operational coastal sand transport models.

### 5.2. Convection Versus Diffusion

[64] *Thorne et al.* [2002] compared the cycle-mean concentration profiles from the present Deltaflume tests with regular waves, and also from tests with irregular waves, with the predictions of *Nielsen*'s [1992] convection-diffusion model. They found that the measured concentration profiles were described rather well by both *Nielsen*'s [1992] "pure convection" and also "combined convection-diffusion" solutions, subject to the reselection of certain model parameters for use above rippled beds. In fact, the mean concentration profiles were described accurately throughout the ABS measurement height range, unlike the present model solutions which tend to become inaccurate above a height of $8\eta$–$10\eta$ (or 0.4–0.5 m).

[65] By interpreting Nielsen's solutions in terms of classical diffusion concepts, *Thorne et al.* [2002] found that the same profile shapes could be obtained if a "constant + linear" (time-invariant) sediment diffusivity (i.e., $K_s \propto$ (constant + $z$)) was assumed from the bed level upward. The inclusion of the lower layer in the present two-layer formulation is broadly consistent with this "constant + linear" modeling approach (in the time-mean sense), the key common element being that each diffusivity tends to a constant mean value either at the bed level, or in a layer that persists right down to the bed level (Figure 11). Thus the approach discussed by *Thorne et al.* [2002] should be viewed as being in the same spirit as that discussed here.

[66] *Thorne et al.* [2002] noted also that while the mean concentration profiles in the Deltaflume experiments could be well represented by use of classical diffusion arguments, a more exacting test of the diffusive approach would involve the modeling of intrawave processes, and specifically the rate at which concentration peaks propagate upward from the bed following vortex shedding at flow reversal. The present study has provided such a test, based on detailed ABS intrawave measurements. As noted earlier (Figures 14 and 15), the upward propagation of the concentration peaks is represented quite well in the lower layer of the model where convection is represented by the new eddy viscosity formulation, but rather less well in the outer layer above this, where a classical turbulent diffusion modeling approach is adopted. Evidently, more work needs to be done on the representation of convection in this layer, and this will be helped when more detailed near-bed velocity measurements become available in the future. However, from a practical point of view, the present model does appear to perform quite well in the near-bed layers of the flow where most of the sand transport occurs.

### 5.3. The β-Factor: Sediment Diffusivity Versus Eddy Viscosity

[67] As noted earlier, a major unresolved issue in the simple 1DV modeling of sand transport above rippled beds concerns the reason why the mean sediment diffusivity ($\overline{K_s}$) is larger than the mean eddy viscosity ($\overline{K}$) by a factor of about 4 times [*Nielsen*, 1992]. This effect has been represented in the present model by the choice $\beta = 4.0$ in the lower layer, with $\beta$ decreasing according to equation (21) in the upper layer.

[68] The explanation of the β-effect requires consideration of the 2DHV (or 3D) velocity and sediment concentration fields. Suppose that in the case of 2DHV flow above ripples, the (phase ensemble) velocity and concentration fields ($u = u(x, z, t)$, $c = c(x, z, t)$) are decomposed initially into mean ($U$ and $C$) and periodic ($u_w$ and $c_w$), ripple-averaged components in the same manner as for 1DV flow (equation (23)). Suppose further that the respective terms are decomposed into terms representing the horizontal mean value ($\langle U\rangle$, etc.) and the deviation from this value ($\tilde{U}$, etc.) over the ripple length, as follows:

$$\begin{aligned} U &= \langle U\rangle + \tilde{U} \qquad C = \langle C\rangle + \tilde{C} \\ u_w &= \langle u_w\rangle + \tilde{u}_w \quad c_w = \langle c_w\rangle + \tilde{c}_w \end{aligned}. \tag{25}$$

[69] It then follows that the horizontal sediment flux at level $z$ is given by

$$\overline{\langle uc\rangle} = \langle U\rangle\langle C\rangle + \langle \tilde{U}\tilde{C}\rangle + \overline{\langle u_w\rangle\langle c_w\rangle} + \overline{\langle \tilde{u}_w\tilde{c}_w\rangle}. \tag{26}$$

Here the first and third terms on the right-hand side are represented in the present 1DV model and are understood, to some extent at least, from observation, while the second and fourth terms are more or less unknown quantities. Similarly, the vertical sediment flux at level $z$ is given by

$$\overline{\langle wc\rangle} = \langle W\rangle\langle C\rangle + \langle \tilde{W}\tilde{C}\rangle + \overline{\langle w_w\rangle\langle c_w\rangle} + \overline{\langle \tilde{w}_w\tilde{c}_w\rangle}. \tag{27}$$

Here the first and third terms on the right-hand side are expected to be zero, since the ripple-averaged vertical velocity components should be zero above a bed that is horizontal (in the mean sense), while the second and fourth terms are, again, more or less unknown quantities. These latter terms represent spatial-temporal correlations between the vertical velocity and sediment concentration fields. Since $\beta > 1$, it may be inferred that in some average sense above a rippled bed, regions of high (or low) concentration are correlated with regions of high (or low) vertical velocity in a way that is different from the correlation that exists between the horizontal and vertical components of velocity. The former correlation determines the sediment diffusivity $K_s$, while the latter correlation determines the eddy viscosity $K$. Another challenge for future work involves the quantifying of these two diffusion rates from detailed 2DHV (or 3D) model and/or experimental results. The recent LES results of *Watanabe et al.* [2003] have suggested a 3D-mechanism, arising from the 3D-instability found by *Hara and Mei* [1990], which may be responsible for enhancing sediment in suspension above long-crested ripples. In other words, the mechanism described above in two dimensions may actually be, to some extent, three dimensional. The earlier LES of *Zedler and Street* [2001] also suggested a 3D-mechanism by which the sediment diffusivity is greater than the eddy viscosity above rippled beds in steady flow. Further insight into 3D effects above ripples has been provided by the direct numerical simulation (DNS) for oscillating flow of *Scandura et al.* [2000]. Using passive tracers, they pointed out a mechanism by which particles are piled up at the ripple crests by the action of the main two-dimensional vortex structures, and then lifted up into the flow by the action of three-dimensional structures. They argued that this mechanism could create additional strong mixing, and increased dispersion.

## 6. Conclusions

[70] A new approach has been presented for the modeling of intrawave sand transport processes above rippled beds beneath weakly asymmetrical waves. The model has been compared with new, detailed ABS (acoustic backscatter system) measurements of the spatial and temporal structure of the suspended concentration field above ripples, made at full scale in the Deltaflume of Delft Hydraulics, Netherlands. The aim of the present study has been to seek a simple one-dimensional vertical (1DV) description of the flow and sediment concentration fields, suitable for practical use. Each aspect of the model has been compared, as far as possible, with the ABS data.

[71] The new, two-layer, 1DV model comprises a lower layer in which the momentum and suspended sediment transfer are dominated by vortex formation and shedding from the ripples, and an upper layer in which turbulent processes are assumed to dominate. The physics of the lower layer is well organized and involves coherent convective processes, while the physics of the upper layer is disorganized, following the break up of the vortices, and involves turbulent diffusive processes. The present intrawave modeling approach differs from previous approaches by its inclusion of a lower convective layer, in which momentum transfer is represented by the eddy viscosity derived for rippled and very rough beds by *Davies and Villaret* [1997, 1999]. This eddy viscosity is qualitatively different from classical eddy viscosity formulations used above flat beds by virtue of having far stronger time variation during the wave cycle and, crucially, peak values in eddy viscosity at times of flow reversal (when vortices are shed from the rippled bed). A sediment pick-up function has been used which also produces peaks in the near-bed sediment concentration at times of flow reversal. Other important features of the model include a prediction scheme for the sand ripple dimensions, based on the empirical approach of *Wiberg and Harris* [1994], and a procedure for the calculation of the suspended sediment grain size from the (assumed known) bed sediment size distribution. The model presented here may be considered to be applicable in the range of relative roughness $1 < A_0/k_s < 4$ and of wave Reynolds number $10^3 < RE < 10^4$ (or $<10^5$ in full-scale conditions).

[72] Ten tests were conducted in the Deltaflume, during two of which a sand ripple (of height about 0.06 m) migrated by a full ripple wavelength during the 1024-s measurement period. This allowed the ABS concentration measurements, recorded in bins of height 0.01 m throughout the bottom 1 m of the flow, to be associated with different "locations" on the ripple surface. The intrawave measurements revealed very clearly the development of sediment "clouds" on the ripple lee slopes, and the disappearance of these clouds at flow reversal following vortex shedding from the bed. The basic entrainment mechanism having been identified, the ABS results have here been ripple-averaged to provide a 1DV concentration field for validation of the present modeling approach.

[73] The observed time-mean concentration profiles are well represented by the present model, as expected since the model has been "tuned" to give the observed vertical decay rate of mean concentration. This has been achieved by use of the parameter $\beta$ that expresses the ratio between the sediment diffusivity and eddy viscosity in the 1DV approach (here $\beta = 4.0$). The focus of the present comparisons is on the modeling of the observed intrawave aspects of the ABS concentration data. Here the model has been found to represent reasonably well both the time variation in the near-bed, ripple-averaged concentration field, and also the variation in phase of the time-varying concentration with height above the bed. The model tends to overestimate the rate of change of phase angle as concentration peaks propagate upward but, nevertheless, captures the physics of the phenomenon in a simple, operational, 1DV model for the first time (at least to the knowledge of the authors).

[74] Owing to the simplicity of the model, many issues remain to be fully resolved; for example, one model improvement would involve the use of a more refined formulation for the change of phase with height in respect to both the eddy viscosity and sediment diffusivity. However, at the present stage of this research, and with the limited amount of high-quality intrawave data that is presently available, it would probably be premature to go directly to a model that is more elaborate than the present one. The present approach seems to provide a promising, computationally inexpensive, means of tackling problems involving not only waves alone, but also combined wave and current flows (as discussed by *Davies and Thorne* [2002]). The present computations of the suspended sediment flux beneath asymmetrical waves have illustrated the ability of the model to quantify the (dominant) "wave-

related" component of the net sand transport, and to shed light on, for example, the sediment sorting processes that are known to occur beneath shoaling waves on beaches.

[75] **Acknowledgments.** Zhihong Li is thanked for his contribution to the initial modeling stages of this work. In addition, the authors particularly acknowledge both Jon J. Williams of POL, who coordinated the experimental work, under contract number MAS3-CT97-0106, and Paul Bell and John Humphery of POL, who carried out and supervised the experimental work. Finally, Jonathan Malarkey is thanked for his help in the preparation of this paper. The modeling work was funded initially as part of the EU MAST3 SEDMOC Project under contract MAST3-CT97-0115, and was completed during the EU 5th Framework SANDPIT Project under contract EVK3-CT-2001-00056.

## References

Andersen, K. H., and C. Faraci (2003), The wave plus current flow over vortex ripples at an arbitrary angle, *Coastal Eng.*, *47*(4), 431–441.

Andersen, K. H., and J. Fredsøe (1999), How to calculate the geometry of vortex ripples, paper presented at Coastal Sediments '99, Am. Soc. of Civ. Eng., Long Island, N. Y.

Andersen, K. H., M. L. Chabanol, and M. van Hecke (2001), Dynamical models for sand ripples beneath surface waves, *Phys. Rev. E*, *63*(6), 066308.

Bailard, J. A. (1981), An energetics total load sediment transport model for plane sloping beach, *J. Geophys. Res.*, *86*(C11), 10,938–10,954.

Bailard, J. A., and D. L. Inman (1981), An energetics bedload model for a plane sloping beach: Local transport, *J. Geophys. Res.*, *86*(C3), 2035–2043.

Block, M. E., A. G. Davies, and C. Villaret (1994), Suspension of sand in oscillatory flow above ripples: Discrete-vortex model and laboratory experiments, in *Sediment Transport Mechanisms in Coastal Environments and Rivers, EUROMECH 310*, edited by M. Bélorgey, R. D. Rajaona, and J. F. A. Sleath, pp. 37–52, World Sci., Hackensack, N. J.

Blondeaux, P., and G. Vittori (1991), Vorticity dynamics in an oscillatory flow over a rippled bed, *J. Fluid Mech.*, *226*, 257–289.

Bosman, J. J. (1982), Concentration measurements under oscillatory motion, report, Delft Hydraul., Netherlands.

Chung, D. H., and L. C. Van Rijn (2003), Diffusion approach for suspended sand transport under waves, *J. Coastal Res.*, *19*(1), 1–11.

Chung, D. H., B. T. Grasmeijer, and L. C. Van Rijn (2000), Wave-related suspended sand transport in the ripple regime, paper presented at 27th International Conference on Coastal Engineering, Am. Soc. of Civ. Eng., Sydney.

Dalrymple, R. A. (1974), A finite amplitude wave on linear shear current, *J. Geophys. Res.*, *79*(30), 4498–4504.

Davies, A. G., and Z. Li (1997), Modelling sediment transport beneath regular symmetrical and asymmetrical waves above a plane bed, *Cont. Shelf Res.*, *17*(5), 555–582.

Davies, A. G., and P. D. Thorne (2002), 1DV-model of sand transport by waves and currents in the ripple bed regime, in *Proceedings of the 28th International Conference on Coastal Engineering*, pp. 2599–2611, World Sci., Hackensack, N. J.

Davies, A. G., and C. Villaret (1997), Oscillatory flow over rippled beds: Boundary layer structure and wave-induced Eulerian drift, in *Gravity Waves in Water of Finite Depth: Advances in Fluid Mechanics*, edited by J. N. Hunt, pp. 215–254, Comput. Mech., Southampton, UK.

Davies, A. G., and C. Villaret (1999), Eulerian drift induced by progressive waves above rippled and very rough beds, *J. Geophys. Res.*, *104*(C1), 1465–1488.

Davies, A. G., and C. Villaret (2002), Prediction of sand transport rates by waves and currents in the coastal zone, *Cont. Shelf Res.*, *22*(18–19), 2725–2737.

Earnshaw, H. C. (1996), A study of flow over a rippled bed using particle image velocimetry, Ph.D. thesis, Univ. of Edinburgh, UK.

Eidsvik, K. J. (2004), Some contributions to the uncertainty of sediment transport predictions, *Cont. Shelf Res.*, *24*(6), 739–754.

Fredsøe, J., and R. Deigaard (1992), *Mechanics of Coastal Sediment Transport*, 369 pp., World Sci., Hackensack, N. J.

Hansen, E. A., J. Fredsøe, and R. Deigaard (1994), Distribution of suspended sediment over wave-generated ripples, *J. Waterw. Port Coastal Ocean Eng.*, *120*(1), 37–55.

Hara, T., and C. C. Mei (1990), Oscillating flows over periodic ripples, *J. Fluid Mech.*, *211*, 183–209.

Houwman, K. T., and B. G. Ruessink (1996), Sediment transport in the vicinity of the shoreface nourishment of Terschelling, report, Dep. of Phys. Geogr., Univ. of Utrecht, Netherlands.

Lee, T. H., and D. M. Hanes (1996), Comparison of field observations of the vertical distribution of suspended sand and its prediction by models, *J. Geophys. Res.*, *101*(C2), 3561–3572.

Lewis, A. W., E. Hitching, G. Perrier, E. A. Hansen, H. C. Earnshaw, K. Eidsvik, C. Greated, B. M. Sumer, and A. Temperville (1995), Flow over vortex ripples: Models and experiments, paper presented at 2nd International Conference on Coastal Dynamics, Am. Soc. of Civ. Eng., Gdansk, Poland.

Li, Z., and A. G. Davies (2001), Turbulence closure modelling of sediment transport beneath large waves, *Cont. Shelf Res.*, *21*(3), 243–262.

Lofquist, K. E. B. (1980), Measurement of oscillatory drag on sand ripples, paper presented at 17th International Conference on Coastal Engineering, Am. Soc. of Civ. Eng., Sydney.

Longuet-Higgins, M. S. (1981), Oscillating flow over steep sand ripples, *J. Fluid Mech.*, *107*, 1–35.

Malarkey, J., and A. G. Davies (2002), Discrete vortex modelling of oscillatory flow over ripples, *Appl. Ocean Res.*, *24*(3), 127–145.

Malarkey, J., and A. G. Davies (2003), A non-iterative procedure for the Wiberg and Harris (1994) oscillatory sand ripple predictor, *J. Coastal Res.*, *19*(3), 738–739.

Malarkey, J., and A. G. Davies (2004), An eddy viscosity formulation for oscillatory flow over vortex ripples, *J. Geophys. Res.*, *109*, C12016, doi:10.1029/2003JC002086.

Marin, F. (1988), Experimental study of the flow generated by water waves above a rippled bed, Ph.D. thesis, Univ. of Le Havre, France.

Mathisen, P. P., and O. S. Madsen (1996a), Waves and currents over a fixed rippled bed: 1. Bottom roughness experienced by waves in the presence and absence of currents, *J. Geophys. Res.*, *101*(C7), 16,533–16,542.

Mathisen, P. P., and O. S. Madsen (1996b), Waves and currents over a fixed rippled bed: 2. Bottom and apparent roughness experienced by currents in the presence of waves, *J. Geophys. Res.*, *101*(C7), 16,543–16,550.

Mathisen, P. P., and O. S. Madsen (1999), Waves and currents over a fixed rippled bed: 3. Bottom and apparent roughness for spectral waves and currents, *J. Geophys. Res.*, *104*(C8), 18,447–18,461.

Nakato, T., F. A. Locher, J. R. Glover, and J. F. Kennedy (1977), Wave entrainment of sediment from rippled beds, *J. Waterw. Port Coastal Ocean Div. Am. Soc. Civ. Eng.*, *103*(WW1), 83–99.

Nielsen, P. (1986), Suspended sediment concentrations under waves, *Coastal Eng.*, *10*(1), 23–31.

Nielsen, P. (1988), Three simple models of wave sediment transport, *Coastal Eng.*, *12*(1), 43–62.

Nielsen, P. (1992), *Coastal Bottom Boundary Layers and Sediment Transport*, 324 pp., World Sci., Hackensack, N. J.

Nielsen, P., and I. A. L. Teakle (2004), Turbulent diffusion of momentum and suspended particles: A finite-mixing-length-theory, *Phys. Fluids*, *16*(7), 2342–2348.

Perrier, G. (1996), Numerical modelling of the transport of non-cohesive sediments by waves and current over a rippled bed, Ph.D. thesis, Orsay Univ., Paris.

Perrier, G., C. Villaret, A. G. Davies, and E. A. Hansen (1995), Numerical modelling of the oscillatory boundary layer over ripples, in *MAST G8-M Coastal Morphodynamics Project: Final Overall Meeting*, pp. 4.26–4.29, Delft Hydraul., Gdansk, Poland.

Ranasoma, K. I. M. (1992), Measurements in combined oscillatory and steady flow over rippled beds, Ph.D. thesis, Univ. of Cambridge, UK.

Ranasoma, K. I. M., and J. F. A. Sleath (1992), Velocity measurements close to rippled beds, paper presented at 23rd International Conference on Coastal Engineering, Am. Soc. of Civ. Eng., Venice, Italy.

Rankin, K. L., and R. I. Hires (2000), Laboratory measurement of bottom shear stress on a movable bed, *J. Geophys. Res.*, *105*(C7), 17,011–17,019.

Rodi, W. (1984), *Turbulence Models and Their Application in Hydraulic—A State-of-the-Art Review*, A. A. Balkema, Brookfield, Vt.

Sato, S., and K. Horikawa (1986), Laboratory study on sand transport over ripples due to asymmetric oscillatory flows, paper presented at 20th International Conference on Coastal Engineering, Am. Soc. of Civ. Eng., Taipei, Taiwan.

Sato, S., K. Shimosako, and A. Watanabe (1987), Measurements of oscillatory turbulent boundary layer flow above ripples with laser-Doppler velocimetry, *Coastal Eng. Jpn.*, *30*(1), 89–98.

Scandura, P., G. Vittori, and P. Blondeaux (2000), Three-dimensional oscillatory flow over steep ripples, *J. Fluid Mech.*, *412*, 355–378.

Sleath, J. F. A. (1973), A numerical model of the influence of bottom roughness on mass transport, in *Numerical Methods in Fluid Dynamics*, edited by C. A. Brebbia and J. J. Connor, pp. 482–493, Pentech, London.

Sleath, J. F. A. (1982), Friction coefficients of rippled beds in oscillatory flow, *Cont. Shelf Res.*, *1*(1), 33–47.

Sleath, J. F. A. (1984), *Sea Bed Mechanics*, 335 pp., John Wiley, Hoboken, N. J.

Sleath, J. F. A. (1987), Turbulent oscillatory flow over rough beds, *J. Fluid Mech.*, *182*, 369–409.
Sleath, J. F. A. (1991), Velocities and shear stresses in wave-current flows, *J. Geophys. Res.*, *96*(C8), 15,237–15,244.
Sleath, J. F. A., and S. Wallbridge (2002), Pickup from rippled beds in oscillatory flow, *J. Waterw. Port Coastal Ocean Eng.*, *128*(6), 228–237.
Smyth, C., A. E. Hay, and L. Zedel (2002), Coherent Doppler Profiler measurements of near-bed suspended sediment fluxes and the influence of bed forms, *J. Geophys. Res.*, *107*(C8), 3105, doi:10.1029/2000JC000760.
Soulsby, R. L. (1997), *Dynamics of Marine Sands: A Manual for Practical Applications*, 249 pp., Telford, London.
Styles, R., and S. M. Glenn (2002), Modeling bottom roughness in the presence of wave-generated ripples, *J. Geophys. Res.*, *107*(C8), 3110, doi:10.1029/2001JC000864.
Svendsen, I. A., and I. G. Jonsson (1980), *Hydrodynamics of Coastal Regions*, 163 pp., Tech. Univ. of Denmark, Lyngby, Denmark.
Swart, D. H. (1974), Offshore sediment transport and equilibrium beach profiles, Delft Univ., Netherlands.
Thorne, P. D., J. J. Williams, and A. G. Davies (2002), Suspended sediments under waves measured in a large-scale flume facility, *J. Geophys. Res.*, *107*(C8), 3178, doi:10.1029/2001JC000988.
Thorne, P. D., A. G. Davies, and J. J. Williams (2003a), Measurements of intra-wave sediment entrainment over a rippled bed, in *Proceedings of Coastal Sediments '03*, East Meets West Prod., Clearwater Fla.
Thorne, P. D., A. G. Davies, and J. J. Williams (2003b), Measurements of near-bed intra-wave sediment entrainment above vortex ripples, *Geophys. Res. Lett.*, *30*(20), 2028, doi:10.1029/2003GL018427.
Trouw, K., J. J. Williams, and C. P. Rose (2000), Modelling sand resuspension by waves over a rippled bed, *Estuarine Coastal Shelf Sci.*, *50*(1), 143–151.
Trowbridge, J., and O. S. Madsen (1984), Turbulent wave boundary layers: 1. Model formulation and first-order solution, *J. Geophys. Res.*, *89*(C5), 7989–7997.
Van Rijn, L. C. (1993), *Principles of Sediment Transport in Rivers, Estuaries and Coastal Seas*, Aqua, Amsterdam.
Van Rijn, L. C., A. G. Davies, J. Van de Graaff, and J. S. Ribberink (2001), SEDMOC: Sediment Transport Modelling in Marine Coastal Environments, 415 pp., Aqua, Amsterdam.
Villard, P. V., and P. D. Osborne (2002), Visualization of wave-induced suspension patterns over two-dimensional bedforms, *Sedimentology*, *49*, 363–378.
Vincent, C. E., and D. M. Hanes (2002), The accumulation and decay of near-bed suspended sand concentration due to waves and wave groups, *Cont. Shelf Res.*, *22*(14), 1987–2000.
Vincent, C. E., S. W. Marsh, M. P. Webb, and P. D. Osborne (1999), Spatial and temporal structures of suspension and transport over megaripples on the shore face, *J. Geophys. Res.*, *104*(C5), 11,215–11,224.
Watanabe, Y., S. Matsumoto, and H. Saeki (2003), Three-dimensional boundary layer flow over ripples, in *Proceedings of Coastal Sediments '03*, East Meets West Prod., Clearwater, Fla.
Wiberg, P. L., and C. K. Harris (1994), Ripple geometry in wave-dominated environments, *J. Geophys. Res.*, *99*(C1), 775–789.
Williams, J. J., P. S. Bell, L. E. Coats, P. J. Hardcastle, J. D. Humphrey, S. P. Moores, P. D. Thorne, and K. Trouw (1998), Evaluation of field equipment used in studies of sediment dynamics, report, 45 pp., Proudman Oceanogr. Lab., Birkenhead, UK.
Williams, J. J., P. S. Bell, L. E. Coates, N. Metje, and R. Selwyn (2003), Interactions between a benthic tripod and waves on a sandy bed, *Cont. Shelf Res.*, *23*(3–4), 355–375.
Zedler, E. A., and R. L. Street (2001), Large-eddy simulation of sediment transport: Currents over ripples, *J. Hydraul. Eng.*, *127*(6), 444–452.

A. G. Davies, School of Ocean Sciences, University of Wales, Bangor, Anglesey LL59 5AB, UK. (a.g.davies@bangor.ac.uk)

P. D. Thorne, Proudman Oceanographic Laboratory, Joseph Proudman Building, 6 Brownlow Street, Liverpool L3 5DA, UK. (pdt@pol.ac.uk)